Energy & Environmental Science

REVIEW

View Article Online
View Journal | View Issue

Cite this: *Energy Environ. Sci.*, 2015, **8**, 81

A comprehensive review of sodium layered oxides: powerful cathodes for Na-ion batteries

Man Huon Han,[a] Elena Gonzalo,[a] Gurpreet Singh[a] and Teófilo Rojo*[ab]

Received 8th October 2014
Accepted 17th November 2014

DOI: 10.1039/c4ee03192j

www.rsc.org/ees

The room temperature Na-ion secondary battery has been under focus lately due to its feasibility to compete against the already well-established Li-ion secondary battery. Although there are many obstacles to overcome before the Na-ion battery becomes commercially available, recent research discoveries corroborate that some of the cathode materials for the Na-ion battery have indeed indisputable advantages over its Li-ion counterparts. In this publication, a comprehensive review of layered oxides (NaT_MO_2, T_M = Ti, V, Cr, Mn, Fe, Co, Ni, and a mixture of 2 or 3 elements) as a viable Na-ion battery cathode is presented. Single T_M systems are well characterized not only for their electrochemical performance but also for their structural transitions during the cycle. Binary T_M systems are investigated in order to address issues regarding low reversible capacity, capacity retention, operating voltage, and structural stability. As a consequence, some materials already have reached an energy density of 520 mW h g^{-1}, which is comparable to that of $LiFePO_4$. Furthermore, some ternary T_M systems retained more than 72% of their capacity along with over 99.7% Coulombic efficiency for 275 cycles. The goal of this review is to present the development of Na layered oxide materials in the past as well as the state of the art today in order to emphasize the compatibility and durability of layered oxides as powerful candidates for Na-ion battery cathode materials.

Broader context

In order to fulfil today's energy demand, a secondary battery beyond the Li-ion battery must be considered especially for large grid systems. Recently, the Na-ion battery is being focused on for its possibility to replace the Li-ion battery because of the economical aspects and availability of intercalation elements. This article provides a comprehensive overview of Na layered oxides as viable cathodes for the Na-ion battery that has already demonstrated economic advantage, large capacities, and ability to cycle for a long term. Although some aspects remain challenging, recent discoveries strongly support the feasibility of Na layered oxides as powerful candidates for Na-ion batteries.

1. Introduction

Rapidly growing advanced technology is a main theme in the 21st century where everyday life depends on many electronic gadgets that require smaller and more powerful energy storage devices in every new generation. Naturally, the development of Li-ion batteries since the first commercialization in 1991 [1] has been the main focus because of its high energy density and almost every portable device today is operated by various forms of Li-ion batteries. Over the decades the huge commercial success of Li-ion batteries leads to even more investments in Li-ion battery research in order to improve the energy density, safety and manufacturing cost of fully functional units. However recently much attention has been shifted to the Na-ion battery,[2–11] because of the cost effectiveness and geographical distribution of Na. Theoretically speaking, the Na-ion battery may not reach the energy density of the Li-ion battery because Na is more than 3 times heavier than Li and the standard electrochemical potential of Na (2.71 V) is lower than Li (3.04) with respect to SHE. Therefore, more suitable applications of the Na-ion battery would be expected in the presence of a large grid support where the operation cost and longevity of the battery are more important aspects of a whole system.

Among many cathode candidates, layered oxides (NaT_MO_2, T_M = Ti, V, Cr, Mn, Fe, Co, Ni, and a mixture of 2 or 3 elements) offer many advantages due to their simple structures, high capacities, and ease of synthesis. As seen in Fig. 1, a dramatic increase in the number of literature studies published in scientific journals in recent years regarding Na layered oxides reflects particular interest by the scientific community. The feasible electrochemistry was already demonstrated using single T_M layered oxides during the 1980s,[12–19] although the initial investigations resulted in poor specific capacity and low capacity retention which later were proved to be due to poor

[a]CICenergigune, Parque Tecnológico de Álava, Albert Einstein 48, ED.CIC, 01510, Miñano, Spain. E-mail: trojo@cicenergigune.com; Tel: +34 945297108

[b]Departamento de Química Inorgánica, Universidad del País Vasco UPV/EHU, P.O. Box. 644, 48080, Bilbao, Spain. E-mail: teo.rojo@ehu.es; Fax: +34 946013500; Tel: +34 946012458

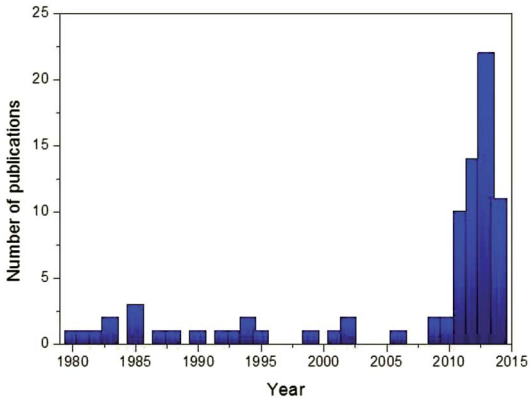

Fig. 1 Evolution of publications related to Na layered oxides by years.

conditions of electrolyte, equipment, *etc.* Over the years, the substitution of electrochemically active or inactive elements into oxide layers, which has been extensively explored during and after the year 2010, has proven to be a versatile approach to address concerns regarding low reversible capacity, poor capacity retention, low operating voltage and structural instability. Incorporating electrochemically active multiple elements activates the redox reaction at a target voltage in order to achieve a smoother charge–discharge profile and higher operating voltage, and utilize more stable de/intercalation reactions. Incorporating a small mole fraction of electrochemically inactive element into an oxide layer could stabilize oxide layers, resulting in better long term cyclability although the amount of Na de/intercalation is reduced by substitution.

Some of the best specific capacities have been achieved with binary T_M systems,[20] which illustrated that an equivalent or even larger energy density compared to commercially available

Dr Man H. Han received his undergraduate degree in Chemistry from the Georgia Institute of Technology in Atlanta. He completed his Ph.D. in Inorganic Materials Chemistry at the Georgia Institute of Technology in 2008, where his thesis focused on synthesis and characterization of magnetic nanoparticles. He has extensive research experience with the synthesis of various inorganic nanomaterials, Li-ion battery materials, surface modification, nanocomposites and their applications. Upon his graduation, he was employed at KaMin LLC as an analytical chemist and is currently working at CIC energiGUNE as a postdoctoral researcher.

Dr Gurpreet Singh received his Ph.D. in the field of lithium ion batteries from the Department of Metallurgical and Materials Engineering, Indian Institute of Technology (IIT) Roorkee in 2009. During his Ph.D., he worked in a multi-institutional project under which he learned prototype fabrication of 18650 and pouch cell design of lithium ion batteries at IIT Kharagpur and first principles' computational studies using VASP at IIT Kanpur. Before joining CIC Energigune he was working as Assistant Manager at Renault Nissan Technology and Business Center India Pvt. Ltd. His current research is focused on process optimization/formulation of electrode materials for secondary batteries.

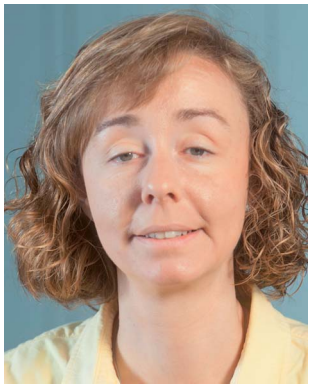

Dr Elena Gonzalo received her Ph.D. in Chemistry from Complutense University (UCM), Madrid, in 2011 under the supervision of Professor Flaviano García-Alvarado and Dr Alois Kuhn on the study of Transition Metal Fluorides and Chlorides as electrodes for lithium batteries with high specific energy. During her Ph.D., she did several research stays in European Universities such as Uppsala University (Sweden), University of Tubingen (Germany) and University of Bath (United Kingdom). After that period, she spent one year working as a postdoctoral researcher at Universidad San Pablo CEU and at Complutense University. She is currently working at CICenergigune as a postdoctoral researcher.

Prof. Teófilo Rojo received his Ph.D. from the University of the Basque Country in 1981. He has spent various research periods at several European and American universities. Since 1992 he has been Full Professor of Inorganic Chemistry at the UPV-EHU. His research has been focused on solid state chemistry and materials science. Since 2010 he has been the Scientific Director of the CIC EnergiGUNE and his research is focused on the study of materials for both lithium and non-lithium based batteries. He holds different positions in various scientific bodies in Spain being the chairman of the Solid State Chemistry Group within the Spanish Royal Society for the last ten years.

Li-ion cathodes could be possible with Na layered oxides. Electrochemical Li–Na ion exchange of Li-rich layered oxides showing capacity as high as 200 mA h g^{-1},[21,22] excellent capacity retention over a long term cycling achieved by structurally stabilized layered oxides,[23] and successful demonstration of full cells utilizing hard carbon as the anode[24,25] all contributed to the development of the idea of commercial Na-ion batteries. Probably increasing the average operating voltage is one of the biggest challenges remaining today although some of the substituted systems exhibited the potential to address this issue in the near future.[26]

2. Structure and nomenclature

Layered oxides of general formula $Na_xT_MO_2$ are composed of repeating sheets of T_MO_6 layers with Na ions being sandwiched in between the oxide layers. Typical Na layered oxides can be synthesized in O3-, P2-, and P3-phases depending on the surrounding Na environment and the number of unique oxide layer packings.[27] The letter indicates the environment where Na is located (O: octahedral, P: prismatic) and the number indicates the number of unique interlayers that are surrounded by different oxide layers. The use of prime (′) indicates a distorted phase. In the O3-phase, mainly known to occur when $0.7 \leq x \leq 1$, oxide layer stacking follows the ABCABC pattern and all Na shares one edge and one face (Fig. 2a). In the P2-phase, mainly known to occur when $x \approx 0.7$, oxide layer stacking follows the ABBA pattern and all Na shares either entirely edge or entirely face (Fig. 2b). In the P3-phase, mainly known to occur when $x \approx 0.5$, oxide layer stacking follows the ABBCCA pattern and all Na shares one face with a T_MO_6 octahedron and three edges with three T_MO_6 octahedra (Fig. 2c).

Electrochemical behaviours are heavily influenced by the structure of the phase not only because of the amount of Na in the pristine state but also due to the stability of each layer and kinetics affected by the surrounding environment of Na. For example, the O3-phase normally undergoes a series of phase transitions due to slab-gliding during the electrochemical cycling.[28] Generally speaking, a better overall electrochemistry is achieved with the P2- than the O3-phase at or beyond the 2nd cycle because of the low diffusion barrier and high ionic conductivity[5,29,30] although the O3-phase normally exhibits a much higher 1st charge capacity because of higher Na contents in the pristine state. Also, the P2-phase is considered to be structurally more stable than the O3-phase because the O3-phase may undergo a series of slab gliding during the de/intercalation process at room temperature. However, a recent study showed that the transition from P2 to O2 is also possible if an extensive amount of Na is deintercalated from the host structure,[31] which implies the structural instability of layered oxides at a deep charge state.

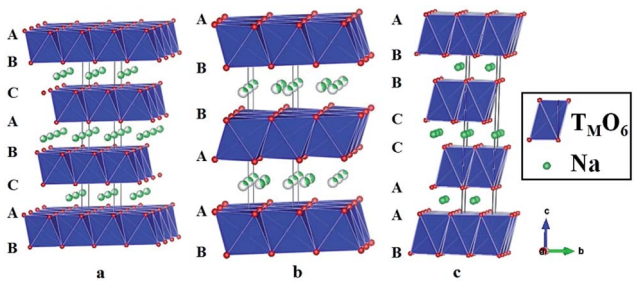

Fig. 2 Typical structure of (a) O3-, (b) P2-, and (c) P3-phase layered oxides.

3. Single T_M systems: $Na_xT_MO_2$

Single T_M systems are mainly studied for obtaining feasible electrochemistry, and each T_M element shows quite unique electrochemical performance regarding reversible capacity, capacity retention, voltage range, and cyclic profile because kinetics involved in the electrochemical process are heavily influenced by the crystallographic phase, structural stability, spin state, electron localization, *etc.* However, some of the unary systems exhibit excellent reversible electrochemistry in a fairly high voltage range with good kinetics, and are the basis of other complex systems.

3.1 Na_xTiO_2

The focus of the initial studies on sodium titanates was to decrease the operating electrochemical potential window because of the possible oxidation of propylene carbonate by highly oxidizing properties of transition metals such as Cr, Co or Ni.[15] Reversible sodium de/intercalation was observed only within $0.7 \leq x \leq 1$ using $NaClO_4$ in PC as an electrolyte, and irreversible capacity loss along with 2D to 3D structural transition was observed for $x < 0.7$. During the charging process, the irreversibility is expected due to the migration of the titanium ions into the interlayer space through the triangular oxygen window, which leads to an increase in polarization because such a process requires high energy. Due to the highly reducing properties of $NaTiO_2$, slow reduction of the liquid electrolyte was also observed and a fully sodiated phase could not be possible during the discharge process even though the integrity of the structure is maintained up to $x \approx 0.7$. A small monoclinic distortion (O′3) from the ideal O3-phase occurred in the slightly sodium deficient phase (Fig. 3).

3.2 Na_xVO_2

Two phases of sodium vanadium oxide, $NaVO_2$ and $Na_{0.7}VO_2$ synthesized by a solid-state reaction, have been studied for their structure and electrochemistry.[32] O3-phase $NaVO_2$ forms a distorted monoclinic structure while P2-phase $Na_{0.7}VO_2$ crystallizes with $P6_3/mmc$ space group symmetry. Despite the multiple plateau behavior, the charge–discharge curves of both phases show a highly reversible electrochemical process (~0.5Na) with the P2-phase having less polarization than the O3-phase (Fig. 4a and c) within the voltage range of 2.4–1.2 V at $C/20$. The derivative curves of both phases (Fig. 4b and d) are significantly different, indicating that the de/intercalation mechanisms are different.

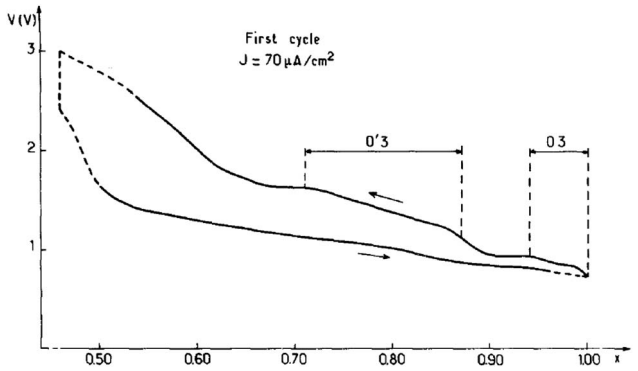

Fig. 3 First cycle charge–discharge curve of $NaTiO_2$ with 3.0 V as upper cutoff. Reprinted with permission from Springer: A. Maazaz, C. Delmas and P. Hagenmuller, *J. Inclusion Phenom.*, 1983, **1**, 45–51. Copyright 1983.

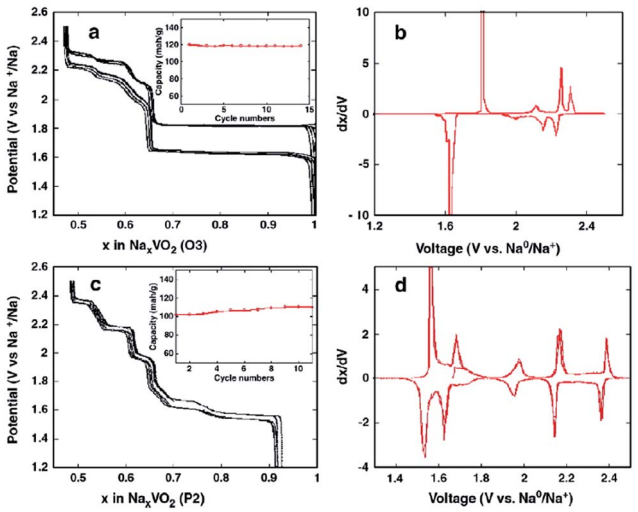

Fig. 4 Voltage–composition curves for (a) $NaVO_2$(O3); (c) $Na_{0.7}VO_2$(P2) and associated, respectively (b) and (d), derivative curves. Insets indicate the capacity evolution *vs.* number of cycles. The cells using 5 to 6 mg of positive electrode composites were cycled at *C*/20. The small polarization between charge and discharge for the P2 phase suggests a high rate capability. This was confirmed by power rate measurements (*e.g.* signature curves) as this electrode can deliver 90% of its capacity at the C rate (1 Na^+ in one hour). Reprinted with permission from Elsevier: D. Hamani, M. Ati, J.-M. Tarascon and P. Rozier, *Electrochem. Commun.*, 2011, **13**, 938–941. Copyright 2011.

In addition, the *in situ* XRD study of P2-phase $Na_{0.7}VO_2$ revealed that the phase remains stable for the whole range while undergoing a series of complex cell parameter evolutions.

More detailed structural change of P2-phase $Na_{0.71}VO_2$ has been investigated by cycling within the voltage range of 2.5–1.4 V at *C*/100 (reversible capacity of 110 mA h g^{-1} and small polarization) while monitoring the phase transition using the *in situ* XRD technique.[33,34] The studied voltage window limit lies in between the anode and cathode for sodium ion batteries and therefore the implementation of such materials as electrodes is difficult to be realized or restricted to anodes for high voltage sodium ion cathodes. Four biphasic regions and three monophasic domains are displayed in the $0.5 \leq x \leq 0.9$ range while three ordered phases at $x = 1/2$, 5/8, and 2/3 appeared, and clear indication of superstructures or modulated structures is evidenced by extra peaks in Fig. 5.

In the meantime, O3-phase Na_xVO_2 obtained by chemically reducing $NaVO_3$ in an H_2 atmosphere[35] has shown a similar phase transition behavior to that of the directly synthesized O3-phase. As seen in Fig. 6a, single phases at $x \approx 0.5$, 0.67, and 1.0 are observed during the cycling, and significant polarization along with not fully relaxed states at particularly around $x \approx 0.5$ and 0.67 (Fig. 6b) was recognized even after a long relaxation which implies low kinetics. The difference in the polarization between the O3 and P2 phases could be considered due to the different Na^+ ion diffusion mechanism within the crystal structure. In the O3 type structure Na^+ ions move through the interstitial tetrahedral site, which is difficult for the larger Na^+ ion, whereas in the case of the P2 type structure Na^+ ions are expected to pass through a lower diffusion barrier. The reversible capacity reached 126.4 mA h g^{-1} within the voltage range of 2.5–1.4 V at *C*/100.

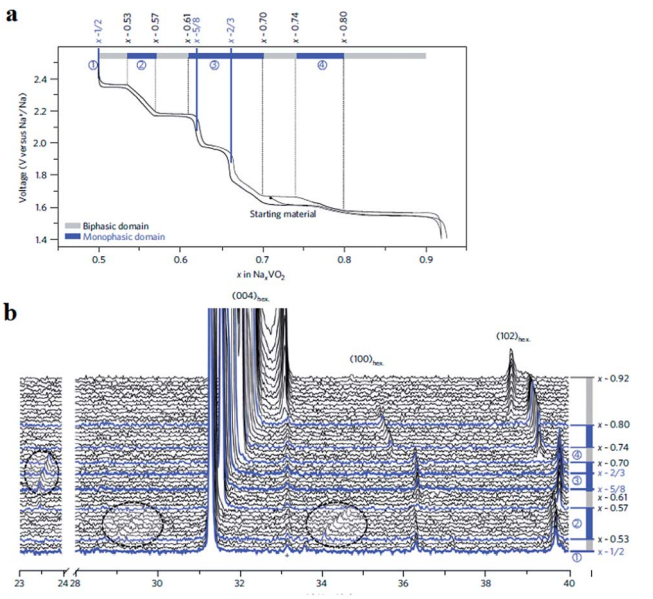

Fig. 5 Evolution of the electrochemical behaviour of the P2-Na_xVO_2 system. (a) Evolution of cell voltage as a function of sodium content in Na_xVO_2 over the $0.5 \leq x \leq 0.92$ range. Biphasic domains and the solid solution regions are shown by dashed lines. Monophasic domains for $x = 1/2$, 5/8 and 2/3 are shown by thick blue lines. (b) *In situ* X-ray diffraction data recorded during the galvanostatic intermittent titration technique experiments. Considering the basic structural model with hexagonal $P6_3/mmc$ symmetry, the main peaks correspond to (004) hex:, (100)hex: and (102)hex: reflections. The Bragg peak centred on 33° corresponds to the V_2O_3 impurity (marked by an asterisk). Additional weak Bragg peaks are visible within the 2θ-range 23.4–23.8° ($0.61 < x < 0.70$) and within the 2θ-ranges 28.9–29.8° and 33.8–34.7° ($0.5 < x < 0.57$). Reprinted with permission from Nature Publishing Group: Guignard, C. Didier, J. Darriet, P. Bordet, E. Elkaïm and C. Delmas, *Nat. Mater.*, 2013, **12**, 74–80. Copyright 2013.

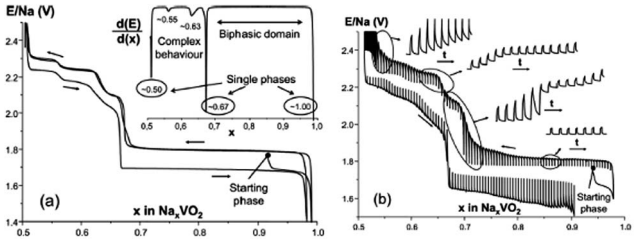

Fig. 6 (a) Electrochemical cycling of Na_xVO_2 ($x = 0.92$ as determined by the lever rule) in the range of 1.4–2.5 V at rate *C*/100. The inset shows the differential curve of the first charge. "Na_xVO_2" is a mixture of $NaVO_2$ and $Na_{2/3}VO_2$. (b) After a first discharge to 1.5 V, electrochemical cycling of Na_xVO_2 ($x = 0.94$ as determined by the lever rule) in GITT-mode (30 min charge–discharge and 2 h relaxation per step) at *C*/100. Insets show the time-dependent variation of the curve at various compositions. Reprinted with permission from The Electrochemical Society: C. Didier, M. Guignard, C. Denage, O. Szajwaj, S. Ito, I. Saadoune, J. Darriet and C. Delmas, *Electrochem. Solid-State Lett.*, 2011. **14**, A75–A78. Copyright 2011.

3.3 Na_xCrO_2

Electrochemistry of Na_xCrO_2 was investigated as early as 1982 where only 0.15Na could be reversibly cycled.[13] However, reinvestigation of the same material revealed that approximately 120 mA h g^{-1} discharge capacity (~0.48Na) could be achieved with a nearly flat voltage profile at 3 V within the voltage range of 3.6–2.0 V at a current density of 25 mA g^{-1} (Fig. 7a) while the Li analogue does not exhibit much of electrochemistry except the 1st charge capacity of 55 mA h g^{-1}.[36] The rate capability study (Fig. 7b) showed that at higher current density, the reversible capacity and the capacity retention improved, which is speculated to be due to an accelerated oxidative decomposition of the electrolyte solution at low current density.

In order to show the feasibility of Cr containing layered oxides as possible cathodes for Na-ion batteries, the reactivity of Na_xCrO_2 against the electrolyte and its thermal stability have been investigated.[37] While undergoing phase transitions of O3(hexagonal)–O3(monoclinic)–P3(monoclinic) the pristine material delivered a capacity of approximately 110 mA h g^{-1} within the voltage range of 3.6–2.0 V at a current density of 25 mA g^{-1} (Fig. 8).

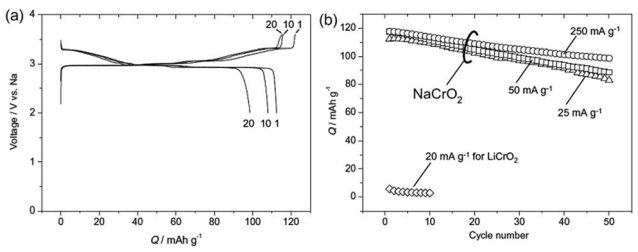

Fig. 7 Galvanostatic charge and discharge curves of (a) a Na||$NaCrO_2$ cell at 25 mA g^{-1} between 2.0 and 3.6 V, and (b) variation in discharge capacity for Li||$LiCrO_2$ and Na||$NaCrO_2$ cells with 1 mol dm^{-3} $NaClO_4$ PC solutions. Reprinted with permission from Elsevier: S. Komaba, C. Takei, T. N., A. Ogata and N. Yabuuchi, *Electrochem. Commun.*, 2010, **12**, 355–358. Copyright 2010.

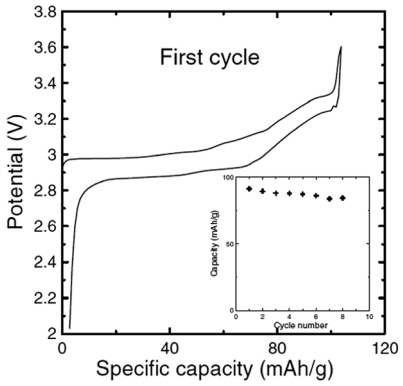

Fig. 8 Electrochemical charge–discharge curves of a Na/$NaCrO_2$ half-cell in 3.6–2.0 V at 25 mA g^{-1}. Specific capacity *versus* cycle number is shown in the inset. Reprinted with permission from The Electrochemical Society: X. Xia and J. R. Dahn, *Electrochem. Solid-State Lett.*, 2011, **15**, A1–A4. Copyright 2011.

The self-heating rate *vs.* temperature plot of $Na_{0.5}CrO_2$ (a partially charged product) in EC–DEC solvent exhibited no measurable exothermic heat in the temperature range of 50–350 °C as seen in Fig. 9 although $Li_{0.5}CoO_2$ and Li_0FePO_4 showed reactivity at 120 °C and 300 °C, respectively. The high stability of Li_0FePO_4 is considered to be due to the strong bond between the O^{2-} and P^{5+} but still some reactivity has been observed at high temperature. ARC (accelerated rate calorimetry) with solvent and TGA experiments for $Na_{0.5}CrO_2$, in which

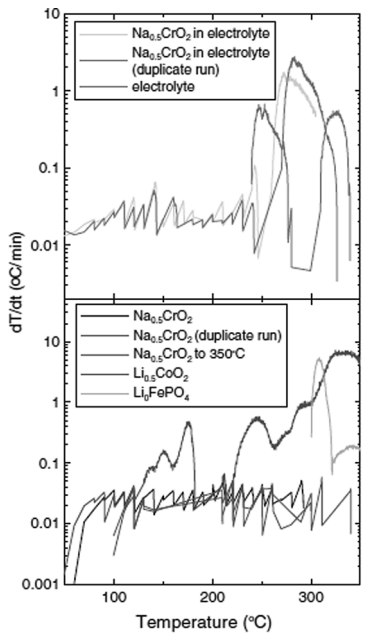

Fig. 9 Self heating rate (SHR) *vs.* temperature of 100 mg $Na_{0.5}CrO_2$, $Li_{0.5}CoO_2$ or $LiFePO_4$ in the same mass of EC–DEC (1 : 2 v/v) or 1 M $NaPF_6$ in EC–DEC (1 : 2 v/v), and the electrolyte itself. The legend indicates which curve corresponds to which sample. Some experiments on $Na_{0.5}CrO_2$ were repeated three times as indicated. Reprinted with permission from The Electrochemical Society: X. Xia and J. R. Dahn, *Electrochem. Solid-State Lett.*, 2011, **15**, A1–A4. Copyright 2011.

no mass loss was observed below 400 °C, confirmed little or no side reaction. On the basis of the XRD and ARC experiments the following reaction mechanism has been proposed:

$$Na_{0.5}CrO_2 \xrightarrow{\text{solvent, }\Delta} 1/2NaCrO_2 + CrO_{2-\delta},$$

which shows very less release of oxygen. In addition, the same plot of $Na_{0.5}CrO_2$ in 1 M $NaPF_6$/EC:DEC exhibited an excellent stability up to 250 °C where only a small amount of heat is released, which is suggested to be due to electrolyte component interactions.

Furthermore, a carbon coating strategy has been incorporated to improve the electrochemical performance of the $NaCrO_2$ cathode.[38] The electron microscopy study revealed homogeneous carbon coated particles of $NaCrO_2$ along with a large amount of carbon trapped in between the particles. With smaller polarization, the carbon coated cathode delivers the charge–discharge capacity of 135/116 mA h g^{-1} at a current density of 5 mA g^{-1}. In the meantime, the naked cathode delivers 125/106 mA h g^{-1} at a similar current density while having the same shape of the cyclic profile (Fig. 10a). Evidenced by anodic and cathodic peaks being closer to each other and having better symmetry in CV (Fig. 10b), the carbon coated cathode exhibits better reversibility and faster diffusion. Also, the carbon coated cathode maintains superior capacity retention by losing only 0.16% per cycle while the naked cathode loses 0.32% per cycle (Fig. 10c).

It is suggested that the improved electrochemical performance is related to the (1) suppression of the side reaction, (2) slowing down of the SEI formation, and (3) increased electronic conductivity as seen in Li-ion battery materials.

The development of the sodium ion battery has followed the footprints of the lithium ion battery development and in this regard commonly used organic electrolytes such as $NaClO_4$ or $NaPF_6$ in carbonate based solvents are usually studied, which are similar to their lithium synonymous $LiClO_4$ or $LiPF_6$. However such electrolytes are considered to be highly volatile and flammable and hence pose a safety risk. Therefore to overcome the drawbacks of the organic based electrolytes, the intermediate temperature ionic liquids have been studied. The electrochemical performance of $NaCrO_2$ has also been tested in ionic liquids, NaFSA–KFSA (FSA: bis(fluorosulfonyl)amide) at 363 K.[39] The charge–discharge profile (Fig. 10a) exhibits a large specific capacity of 113 mA h g^{-1} within the voltage range of 3.5–2.5 V at a current density of 125 mA g^{-1}. As evidenced by *ex situ* XRD, the pristine material undergoes a series of phase transitions, O3–O′3–P′3 during the cycling. The capacity is maintained at 63 mA h g^{-1} for a high current density of 2000 mA g^{-1} (Fig. 11a). The excellent cycling performance, approximately 98% capacity retention and 99.6% Coulombic efficiency at the 100th cycle at a current density of 125 mA g^{-1}, clearly indicates the good stability of $NaCrO_2$ at intermediate temperatures (Fig. 11b).

3.4 Na_xMnO_2

Na_xMO_2, one of the earliest and most characterized layered oxides,[17] is metallic or semiconducting in nature depending on the M–M bond distance and the d orbital overlapping which is a critical factor to determine the kinetics of the system. Na_xMnO_2 can be categorized into two different types of structures. 3D structures ($x = 0.4$ and 0.44) and 2D structures ($x = 1.0$ and 0.7). The 3D or tunnel structure is investigated for many aspects,[40–44] especially for aqueous electrolytes. However, it will not be focused here because it is out of scope of this review. Among the 2D phases three different structures have been observed *viz.* $Na_{0.7}MnO_{2+y}$ (categorized as P2), α-$NaMnO_2$ and β-$NaMnO_2$ depending on the synthesis conditions and stoichiometry. α-$NaMnO_2$ can be indexed to monoclinic while β-$NaMnO_2$ can be indexed to the orthorhombic phase.[45] In high temperature (900 °C) orthorhombic β-$NaMnO_2$, MnO_2 sheets consist of two stacks of edge-sharing MnO_6 octahedra. When tested electrochemically only 0.22 Na could be reversibly cycled in α and 0.15 Na can be cycled in β-$NaMnO_2$.[17] Low conductivity of Na^+ ions causes a high polarization observed in α-$NaMnO_2$. Further the Jahn–Teller effect decreases the Na^+ diffusion coefficient even more. Low polarization in β-$NaMnO_2$ (not shown) compared to α-$NaMnO_2$ could be due to the observed structural differences.

For P2-phase $Na_{0.7}MnO_2$, all the electrochemical studies have been performed on the oxygen rich hexagonal phases. A solid solution is identified in the range of $0.45 \leq x \leq 0.85$ and

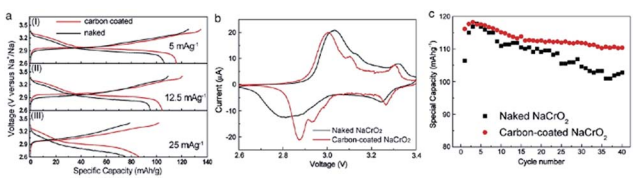

Fig. 10 Galvanostatic curves of $NaCrO_2$/$NaClO_4$/Na cells at a current density of 5 mA g^{-1} (a-I), 12.5 mA g^{-1} (a-II) and 25 mA g^{-1} (a-III); (b) cyclic voltammogram of the $NaCrO_2$/$NaClO_4$/Na cell between 2.6 and 3.4 V at a scan rate of 0.1 mV s^{-1}; and (c) the corresponding specific discharge of the $NaCrO_2$/$NaClO_4$/Na cells at a current of 5 mA g^{-1} as a function of cycle numbers. Reprinted with permission from Elsevier: J.-J. Ding, Y.-N. Zhou, Q. Sun and Z.-W. Fu, *Electrochem. Commun.*, 2012, **22**, 85–88. Copyright 2012.

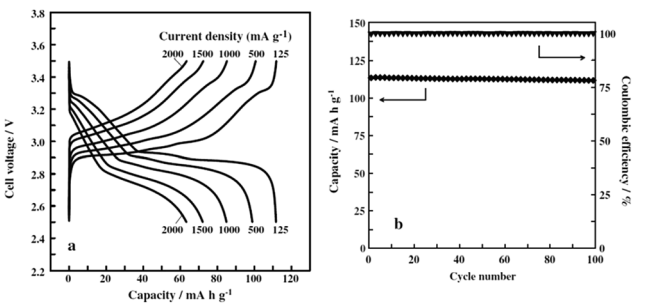

Fig. 11 (a) Charge–discharge curves of the $NaCrO_2$/NaFSA–KFSA/Na cell at different current rates and 363 K in 2.5–3.5 V. (b) Specific discharge capacity and Coulombic efficiency of $NaCrO_2$ in NaFSA–KFSA as a function of cycle number at 125 mA $g^{-1}$and 363 K. Reprinted with permission from Elsevier: C.-Y. Chen, K. Matsumoto, T. Nohira, R. Hagiwara, A. Fukunaga, S. Sakai, K. Jitta and S. Inazawa, *J. Power Sources*, 2013, **237**, 52–57. Copyright 2013.

the P2-phase is maintained during this entire range of electrochemical de/intercalation above 2.0 V (Fig. 12a). The hopping mechanism ($Mn^{3+} \leftrightarrow Mn^{4+}$) is responsible for the conduction in Na_xMnO_2. Further the Jahn–Teller effect of Mn^{3+} increases the electronic localization and a lower diffusion coefficient results due to the Na^+/e^- binding.[17,46]

A close correlation between the defect structure of $Na_{0.7}MnO_2$ and its electronic properties with the electrochemical performance reveals that deviation from the ideal stoichiometry is highly dependent on the synthesis conditions especially temperature and the partial oxygen pressure.[18] Thermogravimetric and thermoelectric power characterizations of the defect structure show that the most probable structural defects are due to the occupancy of some of the sodium sites by the manganese. This leads to the defective structure in both the Na and Mn–O sublattices. This deviation from the ideal stoichiometry in the Mn–O sublattice introduces donor states having ionization energy ≈ 1 eV. Two different samples were studied electrochemically where it has been shown that $Na_{0.7}MnO_{2.02}$ and $Na_{0.7}MnO_{2.18}$ can insert 0.04 and 0.11 moles of Na respectively.

Recently, the electrochemical performance of monoclinic α-$NaMnO_2$ has been reinvestigated,[47] and the charge–discharge capacity during the 1st cycle reached 210 mA h g^{-1} and 197 mA h g^{-1} respectively within the voltage range of 3.8–2.0 V at *C*/10 (Fig. 13a), which decreased to 165 and 149 mA h g^{-1} after 10 cycles. In this study it has been shown that 0.7 Na can be deintercalated up to 3.5 V, which is much higher than α-$NaMnO_2$ studied previously. Even though the exact reasons for such abnormality are not clear, the use of different electrolytes ($NaPF_6$ in EC–DMC in the present case) has been proposed as one of the possible reasons.

When the cell is charged up to 4.2 V, additional charge capacity, mainly due to decomposition of the electrolyte, is obtained. The phase changes in $NaMnO_2$ during the cycling are attributed to Na^+ vacancy ordering or transitions involving the gliding of metal oxygen planes.

P2-phase $Na_{0.6}MnO_2$ with hexagonal crystal structure has been further studied for sodium ion battery cathodes using a PTFE based binder and graphite for cathode mix in conjunction with 1 M $NaClO_4$ in PC as electrolytic solution.[48] As seen in Fig. 14, the similar shape of charge and discharge curves indicates a quasi-reversible de/intercalation process and the discharge capacity reaches 140 mA h g^{-1} within the voltage range of 3.8–2.0 V at a current density of 0.1 mA cm^{-2}. However, due to the severe volume changes during the de/intercalation process, the structure collapses after few cycles.

In addition, the distortion in the Na_xMnO_2 structures is due to the high spin Mn^{3+} Jahn–Teller active ions. The structural investigations regarding Li, Ni and Co doped Na_xMnO_2 reveal that the substitution of Li, Ni and Co leads to the orthorhombic or ideal P2 structure and exposing the sample to air further reduces the degree of distortion.[49] Dopants such as Li, Co and Ni effectively suppress the Jahn–Teller distortion in the structure and hence lead to the ideal undistorted P2 phase even at lower synthesis temperature. Water plays a critical role in the stability of the P2 structure. Exposed and dried $Na_{0.7}MnO_2$ samples have a monoclinic and orthorhombic distortion, respectively, but $Na_{0.7}Mn_{0.85}M_{0.15}O_2$ [M = Co, Ni] has

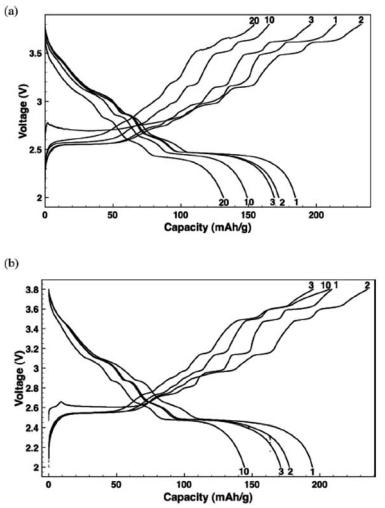

Fig. 13 Voltage profile of $NaMnO_2$ after multiple cycles at *C*/10 (a) and *C*/30 (b) respectively. The cell is galvanostatically cycled between 2.0 V and 3.8 V. Reprinted with permission from The Electrochemical Society: X. Ma, H. Chen and G. Ceder, *J. Electrochem. Soc.*, 2011, **158**, A1307–A1312. Copyright 2011.

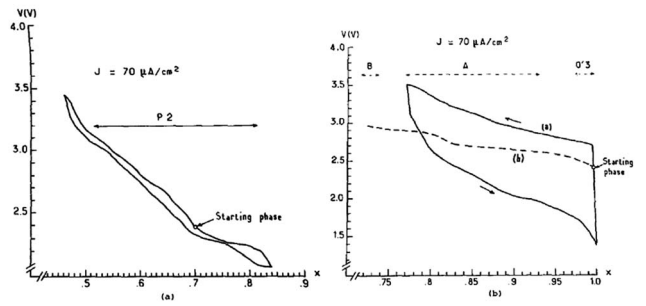

Fig. 12 (a) Electrochemical cycling curve for P2 type $Na_{0.7}MnO_{2.25}$ and (b) α-$NaMnO_2$. Reprinted with permission from Elsevier: A. Mendiboure, C. Delmas and P. Hagenmuller, *J. Solid State Chem.*, 1985, **57**, 323–331. Copyright 1985.

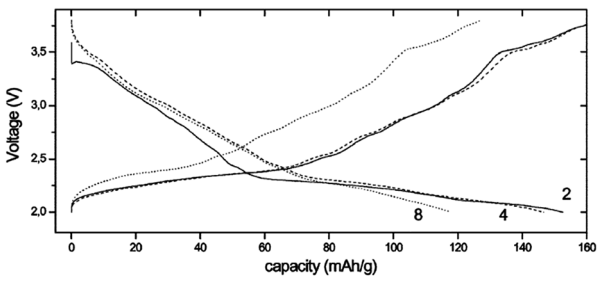

Fig. 14 Charge–discharge curves for an Na/$Na_{0.6}MnO_2$ cell cycled over the voltage range 3.8–2.0 V. Reprinted with permission from The Royal Society of Chemistry: A. Caballero, L. Hernán, J. Morales, L. Sánchez, J. Santos Peña and M. A. G. Aranda, *J. Mater. Chem.*, 2002, **12**, 1142–1147. Copyright 2002.

orthorhombic distortion under both dry and air exposed conditions. Since the lattice parameters did not change drastically after exposing to air, which is expected if water is intercalated between the layers, therefore it is expected that the filling of the vacancies by oxygen and empty sodium sites by the proton could lead to the changes that have been observed.[49] Weakly substituted samples decompose after exposure to boiling water, however heavily substituted samples show comparatively less changes.

In an attempt to increase the electrochemical performance, a nanoplate of $Na_{0.7}MnO_2$ has been synthesized using a hydrothermal method.[50] The nanoplate with uniform size distribution and an average length of about 500 nm along with a width of about 200 nm undergoes a multiple redox process during the cycling, and the CV curves for the first 10 cycles overlap with each other very well except for the 1st cycle, which means that the charge–discharge process after the 2nd cycle is highly reversible. With a small irreversible capacity loss during the 1st discharge process, the capacity reaches 163 mA h g^{-1} within the voltage range of 4.5–2.0 V at a current density of 20 mA g^{-1}.

The discharge capacity is maintained at approximately 150 mA h g^{-1} after 10 cycles at a current density of 40 mA g^{-1} and a good rate capability of 125 mA h g^{-1} discharge capacity at a current density of 180 mA g^{-1} along with the ability to regain a similar discharge capacity when reducing the current density indicates excellent kinetics, indicated by the rate capability experiment.

In an effort to demonstrate a positive effect of partially substituting electrochemically inactive elements for transition metals, Mg^{2+} substituted P2-phase $Na_{0.67}Mn_{1-x}Mg_xO_2$ ($0 \leq x \leq 0.2$) has been investigated where substitution of a small amount of Mn ($x = 0.05$) improves the overall performance without compromising much on the capacity.[51] The charge–discharge profiles became smoother as more Mg^{2+} is substituted for both slowly cooled (Fig. 15a and b) and quenched samples (not shown here) because substitution of Mg^{2+} effectively suppresses the Jahn–Teller distortion of Mn^{3+} by increasing the concentration of Mn^{4+}. At 5% substitution, the initial discharge capacity reaches 175 mA h g^{-1} with moderate capacity retention for 25 cycles and at 20% substitution, the initial discharge capacity reaches 150 mA h g^{-1} along with a capacity retention of 96% after 25 cycles within the voltage range of 4.0–1.5 V at a current density of 12 mA g^{-1}. The plateau above 3.5 V is attributed to the P2–OP4 structural change. Very recently it has been shown that the capacity values can be further pushed beyond 200 mA h g^{-1} by pushing the Mg substitution to achieve the final stoichiometry as $Na_{0.67}Mg_{0.28}Mn_{0.72}O_2$. Such a high capacity, which is beyond its theoretical limit based on the $Mn^{3+/4+}$ redox, is considered to be due to the contribution from oxide ions similar to Li_2MnO_3 based solid solutions for lithium ion batteries.[52]

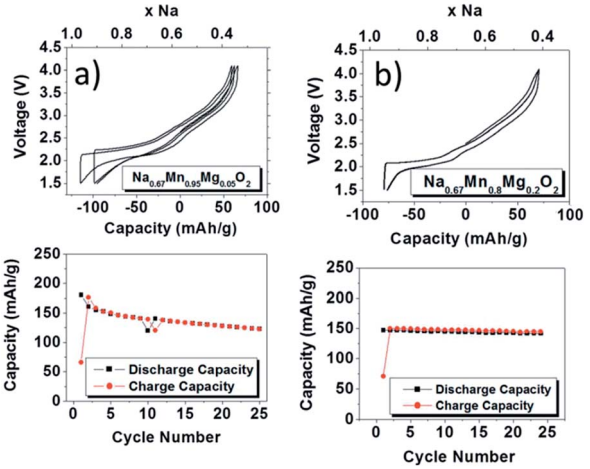

Fig. 15 Electrochemical charge–discharge curves along with cycling performance up to 25 cycles for slow-cooled (a) $Na_{0.67}Mn_{0.95}Mg_{0.05}O_2$ and (b) $Na_{0.67}Mn_{0.8}Mg_{0.2}O_2$. Cycling commenced on charge. The rate was 12 mA g^{-1}. Reprinted with permission from The Royal Society of Chemistry: J. Billaud, G. Singh, A. R. Armstrong, E. Gonzalo, V. Roddatis, C. Armand, T. Rojo and P. G. Bruce, *Energy Environ. Sci.*, 2014, **7**, 1387–1391. Copyright 2014.

3.5 Na_xFeO_2

α- and β-$NaFeO_2$ are well characterized for the phase separation based on the synthesis conditions,[53] and only the low temperature phase, α-$NaFeO_2$, is electrochemically active. In the case of the acid treated $NaFeO_2$, only 0.1Na can be removed from the structure using bromine as an oxidizing agent, yet no chemical reaction has been observed with the less oxidative iodine,[14] which is due to the higher OCV of the α-$NaFeO_2$ than the oxidative potential of iodine. The structure remains unchanged when sodium ions are extracted up to $Na_{0.9}FeO_2$, and Mössbauer spectroscopy proves the presence of Fe^{4+} ions during the deintercalation reaction. The pristine material has higher than 10^8 Ω cm electrical resistivity at room temperature, and $Na_{0.9}FeO_2$ is thermally unstable as it decomposed to stable α-$NaFeO_2$ and Fe_3O_4 above 130 °C.[54] Electrical conductivity can be explained on the basis of the hopping mechanism of the Fe in the octahedral sites through the adjacent empty tetrahedral sites (Fig. 16). α-$NaFeO_2$ has also been tested against the Li anode and a monoclinic structure has been obtained at $Na_{0.5}FeO_2$.[55] The small degree of elongation of the FeO_6

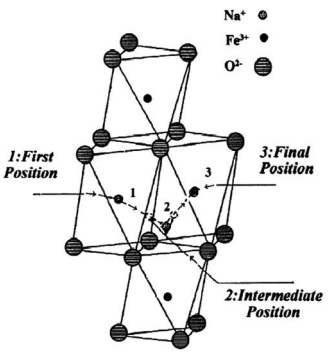

Fig. 16 Sodium ion conduction model in the quasi-bidimensional α-$NaFeO_2$.[57] Reprinted with permission from Elsevier: C. Delmas, A. Maazaz, C. Fouassier, J. M. Reau and P. Hagenmuller, *Mat. Res. Bull.*, 1979, **14**, 329–335. Copyright 1979.

octahedron (compared to the MnO_6 in $NaMn^{3+}O_2$) could be ascribed to the structural compensation for the loss of Na ions rather than by the Jahn–Teller effect of Fe^{4+} ions. Deintercalation beyond $x = 0.5$ was not successful as deintercalation of more than 0.5Na leads to the decomposition of the electrolyte and electrode. A further detailed study on the ionic conductivity has been carried out as well.[56]

Structural and electrochemical characterization of O3-phase α-$NaFeO_2$ has been reinvestigated recently,[58] and the pristine material exhibited a nearly flat voltage profile with an average voltage of approximately 3.3 V. In addition, a systematic cut-off voltage study shows that the electrode performance is highly correlated with the irreversible structural transition when the cut-off voltage is raised above 3.5 V (Fig. 17). Although the charging capacity increases as a function of the cut-off voltage, the reversible capacity decreases when charged beyond 3.5 V. Excellent reversibility with small polarization was observed with the cut-off voltage at 3.4 V. The reversible capacity reaches 100 mA h g^{-1}, indicating that ~0.3Na is reversibly de/intercalated from $NaFeO_2$. The Coulombic efficiency during the first cycle is calculated to be 83% when the cell is charged to 3.4 V, and increases to approximately 97% during the 2nd cycle. Polarization on electrochemical cycles drastically increases after charge to 4.0 V or higher, and the reversible capacity rapidly decreases. Although the electrode becomes electrochemically inactive during the following discharge process, approximately 70% of Na is extracted from O3-phase $NaFeO_2$ by oxidation to 4.5 V by assuming that all current is consumed by the sodium deintercalation reaction without any side reactions. The reversible capacity reaches 80 mA h g^{-1} within the voltage range of 3.4–2.5 V at a current density of 12 mA g^{-1} for 30 cycles.

In an effort to prove the versatility of α-$NaFeO_2$, the thermal stability of α-$NaFeO_2$ is investigated.[59] Partially desodiated $Na_{0.58}FeO_2$ decomposes at or higher than 300 °C and an exothermic peak was detected in a mixture of $Na_{0.58}FeO_2$ and $NaClO_4$/EC–DMC at 220–300 °C using the DSC technique. The pristine cathode delivered an initial capacity of 103 mA h g^{-1} and the following discharge capacity of 85 mA h g^{-1} within the voltage range of 3.6–1.5 V at a current density of 0.2 mA cm^{-2}. The following 2 cycles exhibited nearly 100% Coulombic efficiency with approximately 83 mA h g^{-1} capacity (Fig. 18).

$LiFeO_2$ [60] was found to be electrochemically inactive until 1995 when Kanno and coworkers found that the corrugated $LiFeO_2$ phase was able to extract and insert Li into the structure, although it showed a large capacity decay due to the cation disorder during the electrochemical reaction.

Many efforts have been made to improve the performance of the material such as reducing the particle size[61,62] or coating processes[63] for instance. In the work published by Zhang *et al.*, capacity values of 120 mA h g^{-1} at *C*/10 for the polypyrrole coated material were found after 100 cycles.

The capacity value of $LiFeO_2$ is comparable to the one obtained for $NaFeO_2$, but its average voltage and its capacity retention are higher than the Li counterpart.

3.6 Na_xCoO_2

O3-phase Na_xCoO_2 can be electrochemically deintercalated up to ~0.5Na while undergoing a phase transition to P3 and hence lead to the multiple plateaus in the electrochemical curve in the $0.67 < x < 0.8$ range.[14] The phase transitions during the de/intercalation process were analyzed in more detail using Na_xCoO_2/1 M $NaClO_4$ in PC/Na half-cells as well.[19,64] A series of phases can be synthesized based on the sodium concentration range, O3 ($x = 1$), O′3 ($x = 0.77$), P2 ($0.64 \leq x \leq 0.77$), and P′3 ($0.55 \leq x \leq 0.60$). As seen in Fig. 19, the pristine O3-phase undergoes a series of phase transitions, O3–O′3–P′3, because layers may glide at room temperature as the Na concentration changes. Such a phase transition is also reflected into a large polarization. Starting with the P′3- or O′3-phase, the highest value of x is always obtained with the O3-phase, which implies that the phase transition between O3, O′3, and P′3 is relatively easy process at room temperature.

However, when started with the P2-phase, the P2-phase is preserved over the whole electrochemical range, $0.46 \leq x \leq 0.83$, although multiple plateau behavior is observed due to redistribution of Na^+ (Fig. 20) during the de/intercalation process. A small polarization, indicating structural stability, implies superior long term electrochemical behavior.

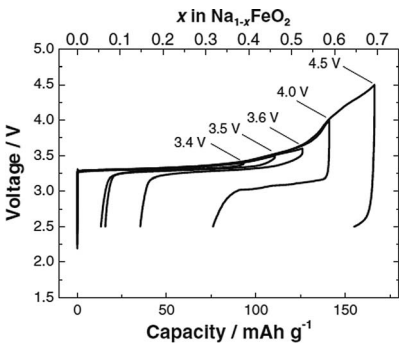

Fig. 17 Initial charge–discharge curves of Na/$NaFeO_2$ cells with different cut-off voltages at a rate of 12 mA g^{-1}. Reprinted with permission from The Electrochemical Society of Japan: N. Yabuuchi, H. Yoshida and S. Komaba, *Electrochemistry*, 2012, **80**, 716–719. Copyright 2012.

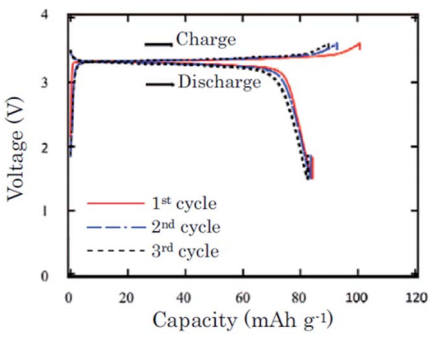

Fig. 18 Charge–discharge profiles of the α-$NaFeO_2$ cathode against the Na anode over the initial three cycles. Reprinted with permission from The Electrochemical Society: J. Zhao, L. Zhao, N. Dimov, S. Okada and T. Nishida, *J. Electrochem. Soc.*, 2013, **160**, A3077–A3081. Copyright 2013.

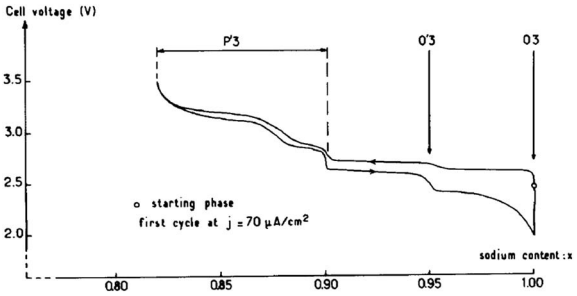

Fig. 19 Emf composition curve obtained from $NaCoO_2$ (03). Reprinted with permission from Elsevier: C. Delmas, J. Braconnier, C. Fouassier and P. Hagenmuller, *Solid State Ionics*, 1981, **3–4**, 165–169. Copyright 1981.

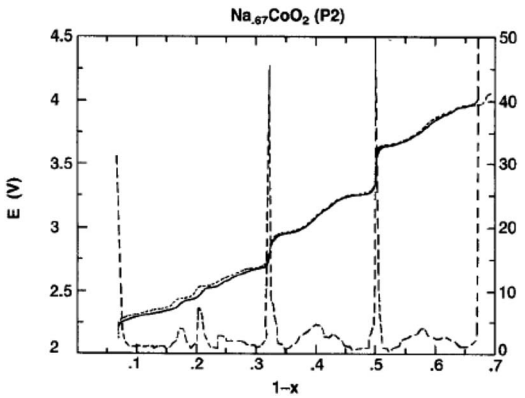

Fig. 20 Open-circuit potential *vs.* composition for P2–$Na_{0.67}CoO_2$ during ion intercalation (solid curve) and deintercalation (dotted curve). Derivative of the OCV curves (dashed curve). Reprinted with permission from The Electrochemical Society: L. W. Shacklette, T. R. Jow and L. Townsend, *J. Electrochem. Soc.*, 1988, **135**, 2669–2674. Copyright 1988.

The cationic redistribution is a consequence of minimizing the electrostatic repulsion between Na^+ ions, the repulsion between face shared Na and Co^{3+} as well as the electron–electron interaction in the oxide layer. Sometimes, only a slight change in Na concentration (1–2%) is enough to induce the redistribution.[65] Precisely designing the experiment, a phase diagram of P2-Na_xCO_2 within the voltage range of 3.1–2.1 V, which constitutes $\sim 0.62 \leq x \leq \sim 0.92$, could be constructed using GITT and *in situ* XRD techniques. A series of ordered phases, $Na_{1/2}CoO_2$ at 3.45 V, $Na_{4/7}CoO_2$ at 3.15 V, and $Na_{2/3}CoO_2$ at 2.80 V along with single phases, $Na_{\sim 0.72}CoO_2$ at 2.56 V, $Na_{\sim 0.76}CoO_2$ at 2.47 V, and $Na_{\sim 0.79}CoO_2$ at 2.38 V, are observed at room temperature as seen in Fig. 21. A temperature dependent experiment reveals that the phase diagram is highly sensitive to the operating temperature, and the feasibility of utilizing electrochemical methods to obtain finely tuned composition materials with good homogeneity is demonstrated as well.

Recently, P2-phase $Na_{0.74}CoO_2$ has been re-evaluated as a feasible cathode material for Na-ion batteries.[66] As seen in Fig. 22a and b, the initial charge capacity reaches 55.7 mA h g^{-1}

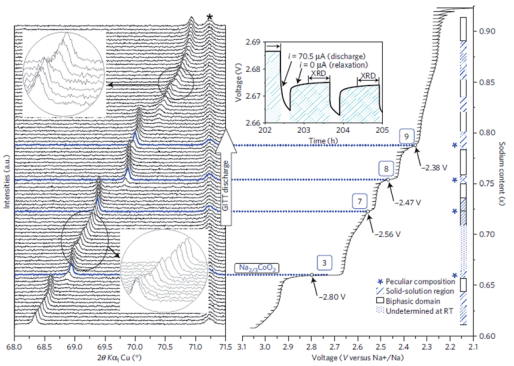

Fig. 21 Synergy between electrochemistry and *in situ* XRD through sodium ion intercalation in P2-Na_xCoO_2. The GITT electrochemical battery discharge (right side) enables the equilibrium potential for each given composition to be obtained. At the end of each relaxation step (top right inset), XRD measurements are carried out to characterize the corresponding system. The resulting *in situ* experiment (left side) clearly evidences that the (008) diffraction peak is shifted to a higher 2θ position, which proves that the interslab distance decreases during sodium intercalation. The biphasic domains are also visible by the splitting of the diffraction lines (tiny splittings are emphasized in the top left and bottom left insets). The (102) diffraction peak of the Be window is marked by the asterisk. The correlation between the electrochemical behaviour and the XRD enables us to draw a new P2-Na_xCoO_2 phase diagram for the $\sim 0.62 \leq x < \sim 0.92$ region that exhibits single-phase domains with either peculiar composition or solid-solution behaviour, and biphasic domains. Reprinted with permission from Nature Publishing Group: R. Berthelot, D. Carlier and C. Delmas, *Nat. Mater.*, 2011, **10**, 74–80. Copyright 2011.

and the following discharge capacity reaches 107.0 mA h g^{-1}, which constitutes a nearly fully sodiated phase, with the polarization range from 150 to 250 mV within the voltage range

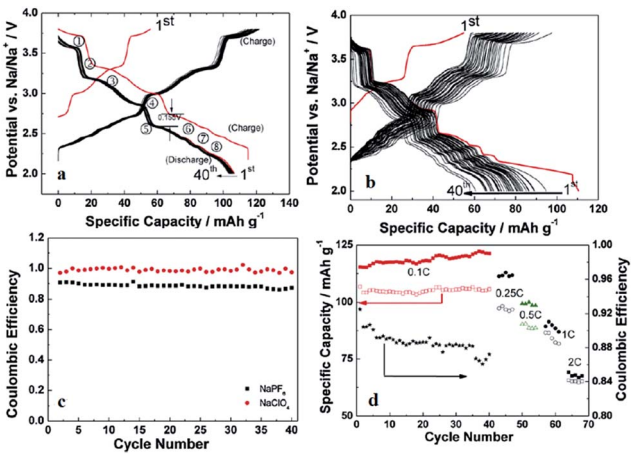

Fig. 22 (a) Galvanostatic curves of P2–$Na_{0.74}CoO_2$/$NaPF_6$/Na cells at a current rate of 0.1 C; (b) galvanostatic curves of P2–$Na_{0.74}CoO_2$/$NaClO_4$/Na cells at a current rate of 0.05 C, and (c) Coulombic efficiency of the cells as a function of cycle numbers. (d) The corresponding Coulombic efficiency and specific discharge and charge capacities of the P2–$Na_{0.74}CoO_2$/$NaPF_6$/Na cells at various current rates of 0.1 C, 0.25 C, 0.5 C, 1 C and 2 C as a function of cycle numbers, the charge capacities and discharge capacities are represented by solid and hollow symbols, respectively. J. J. Ding, Y. N. Zhou, Q. Sun, X. Q. Yu, X. Q. Yang and Z. W. Fu, *Electrochim. Acta*, 2013, **87**, 388–393. Copyright 2013.

of 3.8–2.0 V at 0.1 C. The capacity retention at the 40th cycle is 103 mA h g^{-1} (89% Coulombic efficiency) at 0.1 C and decreases when the *C*/rate increases as it can be observed in Fig. 22d. In addition, the electrode performance based on different electrolytes is studied. As shown in Fig. 22a, when using $NaPF_6$ better cycling performance is observed than when using $NaClO_4$ (Fig. 22b) but $NaClO_4$ provides a better Coulombic efficiency.

A similar system, $Na_{0.71}CoO_2$, is investigated independently.[67] The charge–discharge profile and CV curve (Fig. 23a and d) show a good reversibility of pristine material. Utilizing $NaClO_4$ as the electrolyte, the 1st charge capacity reaches 63.1 mA h g^{-1} while the following discharge capacity reaches 68.7 mA h g^{-1} within the voltage range of 3.5–2.0 V at 0.08 C. Nearly 100% Coulombic efficiency until the 90th cycle (Fig. 23b) is realized. Poor rate capability at high rates (Fig. 23c) is suggested to be due to agglomerates of larger particles.

The same composition, $Na_{0.71}CoO_2$, with different morphology samples are synthesized using Na_2CO_3 (sample I) or NaOH (sample II) and hydrothermally prepared Co_3O_4 nanocrystal.[68] Sample I has a regular platelet shape with sheet edges and flat surface exposed while sample II has an irregular shape with undefined exposed surfaces and broader size distribution. Evidenced by better peak resolution in the CV curve, sample I exhibited faster electrode kinetics because diffusional control of the intercalation element influences the kinetics of the electrochemical process (Fig. 24a and b).

All solid state Na-ion batteries using $Na_{0.7}CoO_2$ synthesized by various techniques have been fabricated using wt% 0.3PEO-0.7PEG as an electrolyte.[69] The solid state reaction produces agglomerated particles of irregular shape with an average size of 8–10 μm, and the ball mill assisted method produces spherical particles with 2–4 μm size. The sol–gel method produces a homogeneous spherical and cylindrical shape with an average size of 500 nm. All samples exhibit a resistivity range of 4–12 mΩ cm, and an initial OCV of 2.7 V which gradually decreases to 2.4 V for solid state cells of all samples. The maximum discharge capacity is found with the sol–gel prepared cathode at approximately 29 μA h (Fig. 25). However, the cells were not cycled further due to the low Na^+ diffusion coefficient (when compared to the Li^+ value in $LiCoO_2$-based systems) and because of the low ionic conductivity of the electrolyte in comparison with the conventional liquid electrolyte.

Other solid state cells, $Na/P(EO)_8NaCF_3SO_3/Na_{0.7}CoO_2$ and $Na_{15}Pb_4/P(EO)_8NaCF_3SO_3/Na_{0.7}CoO_2$, have been investigated at 90–100 °C.[70] At an OCV of 2.8 V, Na de/intercalates in the range of $x = 0.3$–0.9 which produces a volumetric energy density of 1600 W h L^{-1} for Na and 1470 W h L^{-1} for $Na_{15}Pb_4$ within the voltage range of 4.0–1.5 V at a current density of 0.5 mA cm^{-2} as seen in Fig. 26a and b. The multiple plateau behavior is observed, which is characteristic of the P2-phase Na_xCO_2 charge–discharge profile.

Along with good rate capability, more than 60% depth of discharge for 100 cycles and 200 shallower cycles are achieved at a current density of 0.5 mA cm^{-2} as well.

Full Na-ion cells based on Na_xCoO_2 and different carbons have been tested. Depending on the density and the porosity of the carbonaceous material the limit of capacity for sodium insertion has varied. The maximum discharge capacity value of *ca.* 200 mA h g^{-1} in the 4.4–2.5 V range was found for the less dense and highly porous carbon. Sodium ions inserted between the bent layers in the amorphous carbon black and in the pores in the hard carbon were foreseen.[71]

3.7 Na_xNiO_2

The electrochemistry of $NaNiO_2$ was investigated quite some time ago.[12,14,72] O3-phase $NaNiO_2$ forms an ideal hexagonal phase above 220 °C and a distorted monoclinic phase below 220 °C, and for the monoclinic phase, low spin Ni^{3+} induces

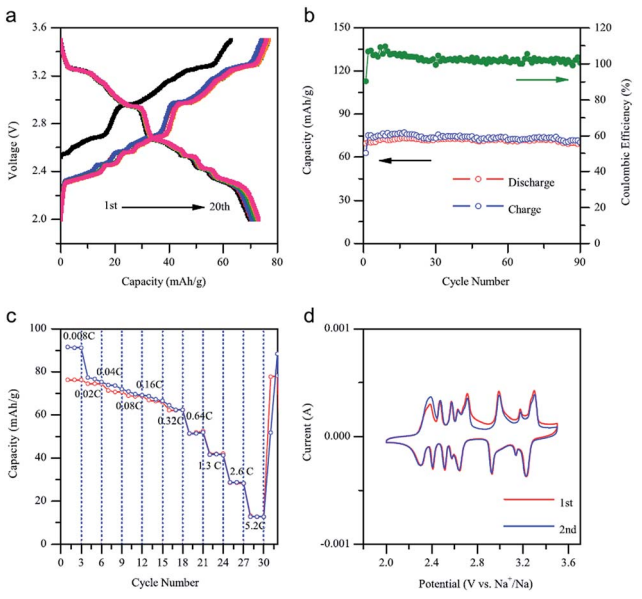

Fig. 23 Electrochemical performances of the $Na_{0.71}CoO_2$ electrode. (a) Charge–discharge voltage profiles between 2.0 and 3.5 V at a current rate of 0.08 C. (b) Capacity retention and Coulombic efficiency plots at a current rate of 0.08 C. (c) The charge–discharge capacity at various *C*-rates is plotted. (d) Cyclic voltammograms at a scan rate of 0.1 mV s^{-1}. Reprinted with permission from Elsevier: A. K. Rai, L. T. Anh, J. Gim, V. Mathew and J. Kim, *Ceram. Int.*, 2014, **40**, 2411–2417. Copyright 2014.

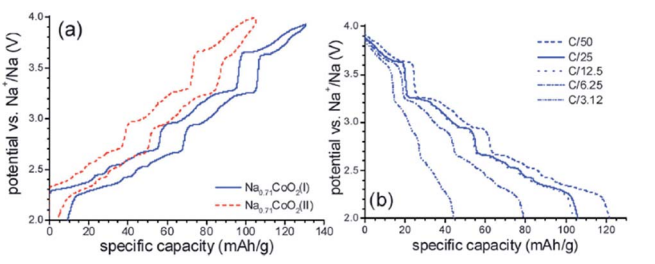

Fig. 24 (a) Charge–discharge curves of $Na_{0.71}CoO_2$ phases in 1.0 M $NaClO_4$ in PC solution at 0.1 mV s^{-1} at a *C*/50 current rate (5th cycle), and(b) discharge current obtained at different current rates (1 C = 249.9 mA g^{-1}) for $Na_{0.71}CoO_2$ (II). Reprinted with permission from The Royal Society of Chemistry: M. D'Arienzo, R. Ruffo, R. Scotti, F. Morazzoni, C. M. Mari and S. Polizzi. *Phys. Chem. Chem. Phys.*, 2012, **14**, 5945–5952. Copyright 2012.

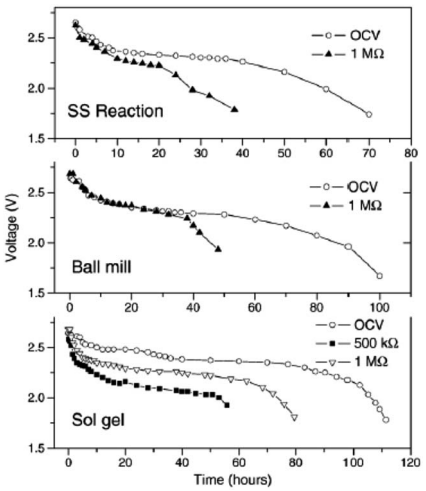

Fig. 25 OCV and discharge characteristics of the $Na_{0.7}CoO_2$ prepared by the solid state reaction, ball milling and sol–gel techniques. Reprinted with permission from Elsevier: A. Bhide and K. Hariharan, *Solid State Ionics*, 2011, **192**, 360–363. Copyright 2011.

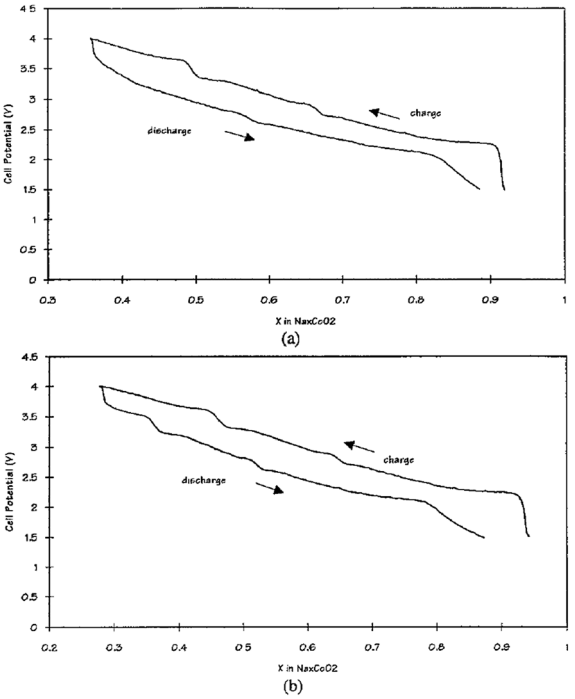

Fig. 26 Cell potentials *vs.* *x* in Na_xCoO_2 in (a) a cell with sodium at 90 °C and (b) a cell with an $Na_{15}Pb_4$ anode at 100 °C. The current density was 0.5 mA cm^{-2} for both charge and discharge. Voltage was plotted as a function of *x* in Na_xCoO_2 based on the amount of charge passed. Reprinted with permission from The Electrochemical Society: Y. Ma, M. M. Doeff, S. J. Visco and L. C. De Jonghe, *J. Electrochem. Soc.*, 1993, **140**, 2726–2733. Copyright 1993.

remarkably strong Jahn–Teller distortion, which creates a deviation of the *a*/*b* cell parameter ratio from an ideal value of 1.73 to 1.86. The potential variations in the electrochemical profiles are related to the Fermi energy and density of the states near the Fermi level. For the temperatures above 600 K the electrical conductivity is almost independent of the temperature, but the activation energy increases from 0.24 eV to 0.36 eV for $x = 1$ to $x = 0.87$ (Fig. 27a). Such an increase in the activation energy and hence decrease in the electronic conductivity are related to the potential jump ΔV in the electrochemical curve (Fig. 27b). Initial investigation of the electrochemical performance of $NaNiO_2$ resulted in deintercalation of only 0.2Na from the crystal.

Recently, O3-phase $NaNiO_2$ was re-evaluated for its electrochemistry.[28] During the 1st cycle, the charge capacity reaches 147 mA h g^{-1} and the following discharge capacity of 123 mA h g^{-1} within the voltage range of 3.75–1.25 V at *C*/10 along with a good capacity retention and the Coulombic efficiency increases to 99.2% after 20 cycles. When cycled between 4.5 and 2.0 V at *C*/10, the 1st charge capacity reached 199 mA h g^{-1} and the following discharge capacity reached 147 mA h g^{-1} as seen in Fig. 28a and b. However, a rapid capacity loss and a low Coulombic efficiency of 86.3% at the 20th cycle are observed. The charge–discharge profile exhibits multiple plateau behaviour due to a series of phase transitions during the cycle. The large capacity loss during the 1st charge–discharge cycle is because a fully sodiated phase could not be reached during the 1st discharge process.

Further details regarding the multiple phase transition during the cycling have been investigated by means of *ex situ* and *in situ* XRD techniques.[73] The charge–discharge profile shows multiple plateaus and the capacity retention is moderate as seen in Fig. 29a and b. The capacity fading has been attributed to the impossibility to recover the pristine distorted O′3-$NaNiO_2$ phase after the first charge–discharge process. The starting point in the subsequent cycles is a new phase denoted as O′′′′3 with 0.83 Na ions per f.u.

The Na concentration during the multiple phase transition is revised based on the electrochemistry and ICP measurement. Unlike previous literature, an observation of a new phase ($Na_{0.83}NiO_2$) at 1.5 V during the discharge process opened up a possibility of obtaining the fully sodiated phase. Recent development of a full cell composed of O3-phase $Na_aNi_{(1-x-y-z)}Mn_xMg_yTi_zO_2$/hard carbon showed a similar electrochemical performance to the commercially available Li-ion battery.[74]

Many other transition metal oxides such as WO_3, ReO_3, MoO_3, VO_2, and V_2O_5 and chalcogenides have also been studied

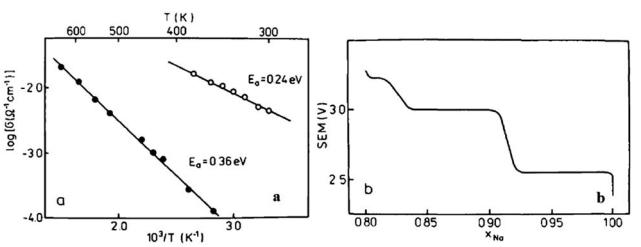

Fig. 27 (a) Temperature dependence of electrical conductivity of $Na_{0.87}NiO_2$ and (b) open circuit voltage of Na_xNiO_2. Reprinted with permission from Elsevier: J. Molenda and A. Stoklosa, *Solid State Ionics*, 1990, **38**, 1–4. Copyright 1990.

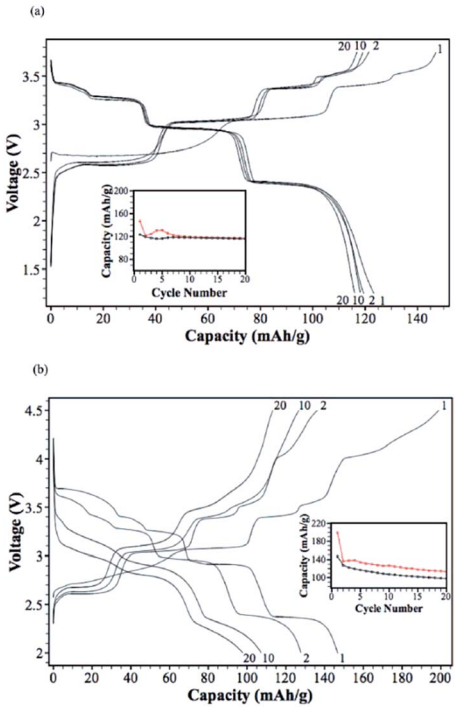

Fig. 28 Voltage profile of $NaNiO_2$ after multiple cycles at *C*/10. The cell is galvanostatically cycled between (a) 1.25–3.75 V and (b) 2.0–4.5 V. Reprinted with permission from The Electrochemical Society: P. Vassilaras, X. Ma, X. Li and G. Ceder, *J. Electrochem. Soc.*, 2013, **160**, A207–A211. Copyright 2013.

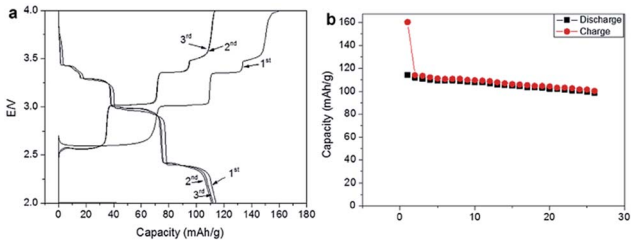

Fig. 29 (a) Voltage *vs.* capacity of Na/$NaNiO_2$ at a *C*/10 rate. (b) Cycling stability and the capacity obtained for $NaNiO_2$ at a *C*/10 rate after 25 cycles. Reprinted with permission from Elsevier: M. H. Han, E. Gonzalo, M. Casas-Cabanas and T. Rojo, *J. Power Sources*, 2014, **258**, 266–271. Copyright 2014.

for Li or Na intercalation during the initial development of electrode materials for sodium and lithium ion batteries and have been summarized in the early review of such materials.[75]

4. Binary T_M systems: $Na_xT_MT'_MO_2$

The cooperative effect of binary metals in metal oxide layers is investigated, and much effort is devoted to removing multiple plateaus, to increasing the average voltage, and to improving the reversible capacity. Among electrochemically active transition metals, combinations of Ni, Fe, Mn, and Co are focused, and some of the best performances including the highest reversible capacity, fairly flat voltage profile, and higher operating voltage are achieved. In addition, substitution of electrochemically inactive elements in the oxide layer proved to enhance the capacity retention and cycling profile while losing some specific capacity.

4.1 $Na_x[NiT'_M]O_2$

Ni containing layered oxides are an interesting system because the overall electrochemical performance is based on the $Ni^{2+/3+/4+}$ redox reaction which has a relatively high operating voltage. However, due to the Jahn–Teller distortion induced by low spin Ni^{3+} ($t_{2g}^6 e_g^1$), the electrochemical cycling profile of the Ni only compound exhibits multiple plateaus during cycling, which is attributed to phase transitions, Na redistribution in the interlayer, or change in the degree of distortion.[73]

The galvanostatic charge–discharge curve of O3-phase $NaNi_{0.5}Mn_{0.5}O_2$ at room temperature shown in Fig. 30a exhibits multiple plateau behaviour[26] while P2-phase $Na_xNi_{1/3}Mn_{2/3}O_2$ shown in Fig. 30b exhibits a smooth charge–discharge curve.[76] The structural evolution investigated by *ex situ* XRD reveals that there are 4 distinctive phase transitions upon charging, and they are determined to be from O3 (pristine) to O′3, P3, P′3, and P″3 which implies multiple slab gliding and a strong Jahn–Teller distortion induced during the cycling. In the meantime, a superior cycling stability is achieved when cycled up to 4.0 V because the P2–O2 phase transition occurs at higher voltage.[77] Obviously, the initial specific capacity of the O3-phase is higher than that of the P2-phase because the initial Na concentration is much higher for the O3-phase, but the

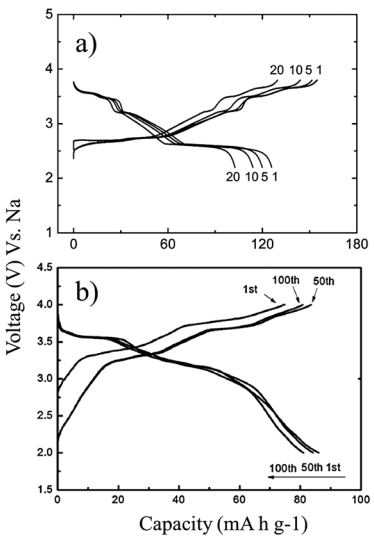

Fig. 30 (a) Galvanostatic charge–discharge curves of sodium/$NaNi_{0.5}Mn_{0.5}O_2$ beaker-type cells at a rate of 1/30 C (8 mA g^{-1}) in the voltage range of 2.2–3.8 V. (b) The voltage profiles of the P2–$Na_{2/3}$-$[Ni_{1/3}Mn_{2/3}]O_2$ cathode cycled between 2.0 V and 4.0 V at 0.1 C. Reprinted with permission from American Chemical Society: S. Komaba, N. Yabuuchi, T. Nakayama, A. Ogata, T. Ishikawa and I. Nakai, *Inorg. Chem.*, 2012, **51**, 6211–6220. Copyright 2012. Reprinted with permission from American Chemical Society: S. Komaba, N. Yabuuchi, T. Nakayama, A. Ogata, T. Ishikawa and I. Nakai, *Inorg. Chem.*, 2012, **51**, 6211–6220. Copyright 2012.

P2-phase exhibits superior capacity retention due to the structural stability. The detailed electrochemical process of the P2-phase $Na_xNi_{1/3}Mn_{2/3}O_2$ within $0 < Na_x < 2/3$ is investigated by combining the first principles computation, electrochemical, and synchrotron techniques.[31] The formation energy calculation and *ex situ* synchrotron XRD indicate that the P2-phase has the lowest energy at $1/3 < Na_x < 2/3$ while the O2-phase becomes more stable as x approaches 0. Evidenced by site occupancy studies coupled with Rietveld refinement, the deintercalation rate of edge shared Na (0.43Na in the pristine state) is slightly faster than the face shared Na (0.25Na in the pristine state) down to $x = 1/3$ where each site is occupied by 0.17Na and the deintercalation rate becomes approximately the same below $x = 1/3$. In addition, the diffusion coefficient calculated by the GITT technique for $1/3 < Na_x < 2/3$ is 7×10^{-9} to 1×10^{-10} cm^2 s^{-1} which is faster than the Li diffusivity in the O3 structure. The capacity retains at only 64% after 10 cycles within the voltage range of 4.5–2.3 V due to the P2–O2 transition, but when cycled below the transition voltage, 92% capacity retention up to 50 cycles along with a good rate capability is obtained.

A series of Fe substituted O3-phase $NaFe_x(Ni_{1/2}Mn_{1/2})_{1-x}O_2$ has been investigated for enhanced electrochemical performance.[78] Although the reversible capacity is reduced to 130 mA h g^{-1} within the voltage range of 3.8–2.0 V at $C/20$, the $NaFe_{0.4}(Ni_{1/2}Mn_{1/2})_{0.6}O_2$ delivered a smooth charge–discharge profile, good capacity retention and rate capability. In addition, Ti substituted P2-phase $Na_{2/3}Ni_{1/3}Mn_{2/3-x}Ti_xO_2$ ($x = 0$, 1/6, 1/3, and 2/3) exhibited the most improved electrochemical performance with the nominal composition of $Na_{2/3}Ni_{1/3}Mn_{1/2}Ti_{1/6}O_2$ at a specific capacity of 127 mA h g^{-1} within the voltage range of 4.5–2.5 V at a current density of 12.1 mA g^{-1}.[79] The concentration of Ti introduces a remarkable structural stability even at such a high cut-off voltage, which is proposed to be due to smaller volume change for heavily substituted compounds, but the reversible capacity becomes smaller because Ti is electrochemically inactive. Furthermore, the electrochemistry of O3-phase $NaNi_{0.5}Ti_{0.5}O_2$ demonstrates the beneficial effect of Ti substitution into Ni containing layered oxides.[80,81] The 1st charge–discharge capacities reached 170/121 mA h g^{-1} within the voltage range of 4.7–2.0 V at 0.2 C, but the capacity retention is low at 52.8% after 50 cycles. When the upper voltage is limited to 4.0 V, however, the first 3 cycles overlap with each other very well, and the excellent capacity retention of 93.2% after 100 cycles is obtained at 0.2 C as seen in Fig. 31a. In addition, an excellent rate capability delivering 27 mA h g^{-1} even at 10 C rate (Fig. 31b) is attributed to the faster Na ion diffusivity in this particular phase.

Recently, electrochemistry of $Na_2Ni_2TeO_6$ and $Na_{1.6}Sr_{0.2}Ni_2TeO_6$ has been evaluated for high voltage cathode materials. $Na_2Ni_2TeO_6$ delivered a maximum discharge capacity of approximately 110 mA h g^{-1} based on the $Ni^{2+/3+}$ redox reaction within the voltage range of 4.35–3.0 V at 0.03 C, and $Na_{1.6}Sr_{0.2}Ni_2TeO_6$ delivered a maximum discharge capacity of 108.5 mA h g^{-1} within the voltage range of 4.35–3.00 V at 0.05 C. However, the electrolyte stability at such a high cut-off voltage remains questionable.

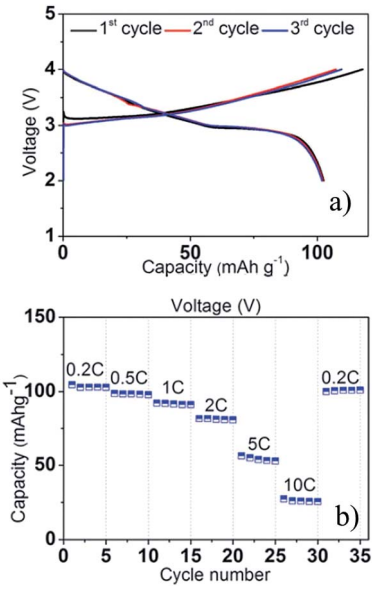

Fig. 31 (a) Initial three charge–discharge voltage profiles of the Na/O3-NNT cells at a current density of 0.2 C in the voltage range of 2.0–4.0 V, and (b) rate performance of the Na/O3-NNT cell at the rates of 0.2 C, 0.5 C, 1 C, 2 C, 5 C and 10 C. Reprinted with permission from The Royal Society of Chemistry: H. Yu, S. Guo, Y. Zhu, M. Ishida and H. Zhou, *Chem. Commun.*, 2014, **50**, 457–459. Copyright 2014.

One of the most significant improvements regarding multiple plateau behaviour was achieved with a Li substituted system.[82] A small substitution of Li in the transition metal oxide layer to yield $Na_{0.85}Li_{0.17}Ni_{0.21}Mn_{0.64}O_2$ vastly improves the charge–discharge profile with an average voltage of 3.4 V. An excellent rate capability with a reversible capacity of 65 mA h g^{-1} at a current density of 1600 mA g^{-1} is achieved, in which the power density at such performance is projected to be 670 W kg^{-1}. The average capacity of 95–100 mA h g^{-1} (approximately 87% of theoretical capacity) is achieved after 50 cycles which is only 2% capacity fade from the initial capacity at a current rate of 15 mA g^{-1} within the voltage range of 4.2–2.0 V. The gradual capacity fade is proposed to be due to the side reaction of the electrolyte with Na metal, electrochemical reduction of the surface oxide species on Na metal and Na plating problem on charge.

A feasibility of full cell Na-ion batteries has been demonstrated using the $NaNi_{0.5}Mn_{0.5}O_2$ cathode and hard carbon anode full cell configuration.[24] Various electrolytes, $NaClO_4$, $NaPF_6$, and $NaN(SO_2CF_3)_2$ (sodium bis(trifluoromethanesulfonyl)amide, NaTFSA) in PC, are evaluated and all systems exhibited more than 200 mA h g^{-1} reversible capacity based on the anode. Multiple plateaus during the cycling are observed, which is characteristic of $NaNi_{0.5}Mn_{0.5}O_2$. The NaTFSA solution exhibits a better cyclic performance after 50 cycles by maintaining more than 70% of capacity, and the same cell tested at 60 °C shows similar cyclic performance. Furthermore, an excellent rate capability even at 300 mA g^{-1} proves the feasibility of Na-ion full cell batteries. At an average operating voltage of 3 V, this type of full cell Na-ion battery achieves *ca.* 60% of the practical energy density of Li-ion batteries.

4.2 $Na_x[FeT'_M]O_2$

Fe containing layered oxides are very appealing from an application point of view because of natural abundance, environmental benignity, and high operating voltage. Coupling with Mn, Co, or Ni has the potential to obtain a high operating voltage and specific capacity. Specifically, Fe coupled with Mn seems to be a promising electrode by exhibiting one of the largest specific capacities along with good capacity retention.[20] However, the challenges lie in (1) irreversible phase change above 3.4 V for α-$NaFeO_2$ [58] and (2) low average potential of the $Mn^{2+/3+/4+}$ redox reaction and (3) possibility of Mn ion dissolution in the electrolyte.[83] The electrochemical performance comparison between partially sodiated P2-phase $Na_{2/3}Fe_{1/2}Mn_{1/2}O_2$ and O3-phase $NaFe_{1/2}Mn_{1/2}O_2$ reveals that the P2-phase exhibits better overall electrochemistry by delivering a reversible capacity of 190 mA h g^{-1} within the voltage range of 4.2–1.5 V at a current density of 12 mA g^{-1} (Fig. 32b) and good rate capability (Fig. 32d) while the fully sodiated O3-phase delivered 100–110 mA h g^{-1} of reversible capacity under the same experimental conditions (Fig. 32a) although the capacity retention rate for both samples is almost identical (Fig. 32c). In addition, the total redox capacity of Fe is different from that of Mn probably because the reversible range associated with the Fe redox reaction is limited by irreversible Fe migration at high voltage.[84] At an average operating voltage of 2.75 V, the energy density is estimated to be 520 mW h g^{-1}, which is comparable to that of the commercially available Li-ion battery cathode.[20,84]

Also, submicron size P2-phase $Na_{2/3}Fe_{1/2}Mn_{1/2}O_2$ cycled within the voltage range of 4.0–1.5 V exhibited an excellent capacity retention of 99.6% for 50 cycles.[85] The electrochemical performance of P2- and O3-phases is further investigated with a series of $Na_xFe_xMn_{1-x}O_2$ ($1.0 \leq x \leq 0.5$).[86] When $x > 0.65$, the O3-phase is stabilized while when $x < 0.65$, a combination of two or more O3- and P2-like phases is formed. The capacity, reversibility, capacity retention and polarization are improved as the Mn concentration increases up to $x = 0.5$. Such an improvement is suggested to be due to hindered cooperative Jahn–Teller distortions by introducing less active Jahn–Teller ions for the mixed metal ions than pure $NaMnO_2$ or α-$NaFeO_2$. In addition, it was observed that when smaller amounts of $Fe^{3+/4+}$ redox were utilized, the capacity fade became less prominent.[87,88] However, the electrochemical performance comparison between P2-phase $Na_{0.67}Mn_{2/3}Fe_{1/3}O_2$, P2-phase $Na_{0.71}Mn_{1/2}Fe_{1/2}O_2$, O3-phase $Na_{0.82}Mn_{1/3}Fe_{2/3}O_2$, and (O3+O′3)-phase $Na_{0.8}Mn_{1/2}Fe_{1/2}O_2$ at $C/100$ showed slightly higher reversible capacity for the P2-phase if the transition metal concentration remains the same (see Fig. 33). However, the reversible capacity of O3-phases here exhibited higher discharge capacity than those reported in the previous studies,[20] which could be due to the transition metal vacancies introduced based on the experimental conditions or Fe migration at high voltage.[58]

Generally the P2 based cathode compositions such as $Na_{2/3}Fe_{1/2}Mn_{1/2}O_2$ have sodium deficient structure. Therefore the full reversible capacity can only be achieved either by using a source of sodium as an anode or by presodiating the cathode. Very recently, an approach based on utilizing a sacrificial salt as a cathode mix demonstrated the feasibility of overcoming the limitation of sodium deficiency in the structure. NaN_3 is used as a sacrificial salt which act as a source of required sodium and gives an irreversible capacity at ~3.5 V which is well within the operating voltage window for most of the P2 based cathodes. The oxidation reaction of NaN_3 is proposed as $2NaN_3 \rightarrow 3N_2 + 2Na^+ + 2e^-$. Due to the high theoretical charge capacity (~412 mA h g^{-1}), a very small amount of NaN_3 is required to overcome the sodium deficiency issue. This approach can be applied to the sodium deficient materials covering the operating voltage window of NaN_3 during the formation step of sodium ion cells.[89,90] Lastly, electrochemically reversible Li intercalation in P′3-phase $Na_{2/3}Mn_{1-y}Fe_yO_2$ ($y = 0$, 1/3, 2/3) has been demonstrated[91] which proves the feasibility of obtaining a high capacity Li-ion cathode from a very stable Na layered oxide.

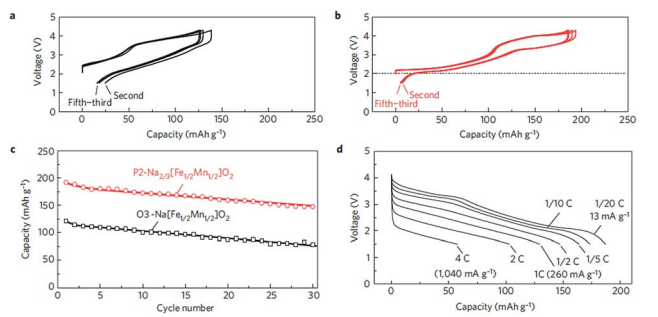

Fig. 32 Galvanostatic charge–discharge (oxidation–reduction) curves for Na/Na[$Fe_{1/2}Mn_{1/2}$]O_2 (a) and Na/$Na_{2/3}$[$Fe_{1/2}Mn_{1/2}$]O_2 (b) cells at a rate of 12 mA g^{-1} in the voltage range of 1.5 and 4.3 V. For the Na/$Na_{2/3}$[$Fe_{1/2}Mn_{1/2}$]O_2 cell, the first charge curve is not shown for simplicity. (c) Comparison of the discharge capacity retention of the sodium cells. (d) Rate capability of a Na/$Na_{2/3}$[$Fe_{1/2}Mn_{1/2}$]O_2 cell. The cell was charged (oxidized) to 4.2 V at a rate of 13 mA g^{-1} and then discharged (reduced) to 1.5 V at different rates of 1/20 (13 mA g^{-1}) to 4 C (1040 mA g^{-1}). The sample loading on Al foil was 8 : 4 mg cm^{-2}. The applied current density was approximately 2.2 mA cm^{-2} at the 1 C rate, which was defined on the basis of one electron redox of the transition metal in the sample (260 mA g^{-1}). Reprinted with permission from Nature Publishing Group: N. Yabuuchi, M. Kajiyama, J. Iwatate, H. Nishikawa, S. Hitomi, R. Okuyama, R. Usui, Y. Yamada and S. Komaba, *Nat. Mater.*, 2012, **11**, 512–516. Copyright 2012.

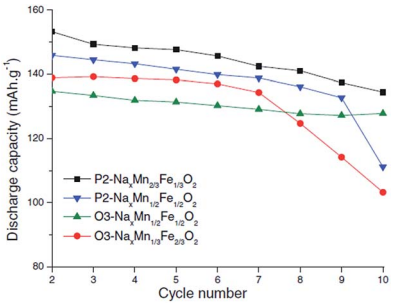

Fig. 33 Evolution of the discharge capacities of the different Na//Na_x(Mn,Fe)O_2 cells. Reprinted with permission from The Electrochemical Society: B. Mortemard de Boisse, D. Carlier, M. Guignard and C. Delmas, *J. Electrochem. Soc.*, 2013, **160**, A569–A574. Copyright 2013.

Coupling Fe with Co or Ni is an interesting combination because of the high flat voltage nature of α-$NaFeO_2$ although there are many challenging aspects mentioned above. O3-phase $NaFe_{0.5}Co_{0.5}O_2$, an intermediate solid solution of $NaFeO_2$ and $NaCoO_2$, delivered 160 mA h g^{-1} reversible capacity within the voltage range of 4.0–2.5 V at a current density of 12 mA g^{-1} as seen in Fig. 34a.[92] The average voltage (3.14 V) is higher than that of $NaFeO_2$ and $NaCoO_2$ along with a smoother charge–discharge profile in a lower voltage range compared to $NaCoO_2$. The capacity retention is improved as well comparing both end members of compounds and is moderate at 85% after 50 cycles (Fig. 34b). A good capacity retention is obtained delivering over 100 mA h g^{-1} at 30 C rate. The *in situ* XRD experiment revealed that a two-phase region for $NaFe_{0.5}Co_{0.5}O_2$ only exists at the beginning of the charge process (O3–P3 transition) and such a good rate capability is proposed to be because of faster Na diffusivity in the P3-phase.

In addition, O3-phase $NaFe_{1-x}Ni_xO_2$ ($0.5 \leq x \leq 0.7$) delivered 112 mA h g^{-1} and 135 mA h g^{-1} with the initial Coulombic efficiency of 89% and 93% (Fig. 35) although the average potential decreased to 2.85 V and 2.7 V for $x = 0.5$ and 0.7, respectively, within the voltage range of 3.8–2.0 V at a current density of 30 mA g^{-1}.[25] Substitution of Fe with Ni largely suppressed polarization during cycles, and the origin of improved electrochemistry is suggested to be due to the introduction of $Ni^{3+/4+}$ redox reactions, which suppresses the Jahn–Teller element effect of Fe^{4+} during the cycle. Very recently, a study on the $NaFe_x(Ni_{0.5}Ti_{0.5})_{1-x}O_2$ ($x = 0.2$ and $x = 0.4$) cathode has shown an improved average potential of ≥3.1 V and a discharge capacity of ~120 mA h g^{-1} in the narrow operating potential window of 3.75–2.6 V, while maintaining the smooth voltage profile. An improved electrochemical performance has been observed for the NaFSI based electrolyte compared to $NaClO_4$, with capacity falling to 83% of its initial value after 30 cycles.

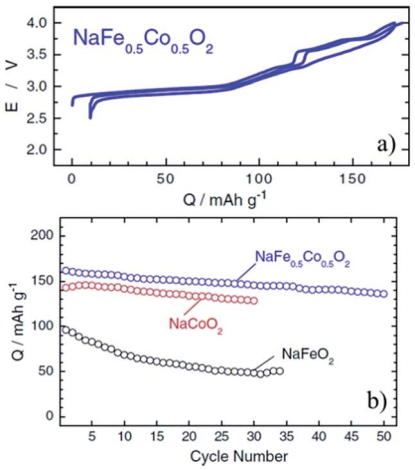

Fig. 34 (a) Charge–discharge curves of $NaFe_{0.5}Co_{0.5}O_2$ in Na cells at a rate of 12 mA g^{-1}. The changes in the discharge capacity for 50 cycles are shown in (b). Reprinted with permission from Elsevier: H. Yoshida, N. Yabuuchi and S. Komaba, *Electrochem. Commun.*, 2013, **34**, 60–63. Copyright 2013.

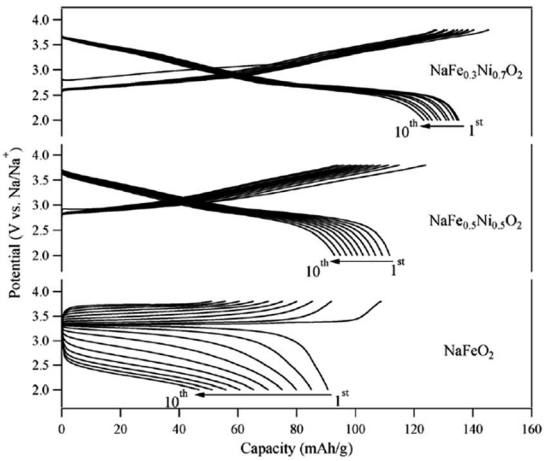

Fig. 35 Charge–discharge curves at a specific current of 30 mA g^{-1} during the initial 10 cycles.

4.3 $Na_x[CoT'_M]O_2$

Co containing Na layered oxide cathodes have many drawbacks including low reversible capacity, multiple plateaus, and rapid capacity fade.[66] Also, Co may not be the best choice for electrochemically active transition metals because of high price and toxicity. Until now, Co coupled with Mn systems, P2-phase $Na_{2/3}Mn_yCo_{1-y}O_2$, have been most extensively investigated. Generally speaking, when the Mn concentration increases, the high voltage capacity decreases ($Co^{4+/3+}$ redox), but the overall capacity slightly increases along with a smother charge–discharge profile (Fig. 36) up to $y = 1/2$.[93–95] The reversible capacity further increases beyond $y = 1/2$, but plateau behaviour reoccurs with larger polarization.

5. Ternary T_M systems and beyond

Carefully designing a complex mixture of electrochemically active transition metals can selectively activate the redox reaction of desired elements at a target voltage. Such a scheme could enable a smooth charge–discharge profile by preventing multiple phase transition or changes in the degree of distortion during the cycling. In addition, tuning the operating voltage, desirably at high voltage, could be possible by understanding the effect of cooperative interactions between the active and spectatorial elements.

5.1 $Na_x[NiFeMn]O_2$

Ni substituted P2-phase $Na_xMn_{1-y-z}Fe_yNi_zO_2$ exhibits a significantly improved electrochemical performance,[96,97] and a stable reversible 2-phase transition is observed using the *ex situ* XRD technique. The improved electrochemical behaviour is proposed to be due to the suppression of Jahn–Teller distortion by reducing the concentration of high spin Mn^{3+}. In addition, substitution of a small amount of Ti leads to long cycling performance.[98] The feasibility of full cells utilizing O3-phase $Na[Ni_{1/3}Fe_{1/3}Mn_{1/3}]O_2$ is demonstrated using hard carbon as an anode.[99] Although some irreversible capacity loss is observed

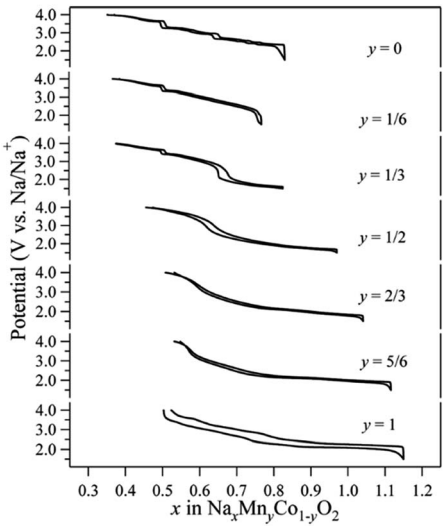

Fig. 36 Charge–discharge curves at a specific current of 30 mA g^{-1}. Reprinted with permission from American Chemical Society: X. Wang, M. Tamaru, M. Okubo and A. Yamada, *J. Phys. Chem. C*, 2013, **117**, 15545–15551. Copyright 2013.

during the 1st discharge process mostly due to the carbon electrode first cycle irreversibility which is caused by the formation of SEI on a hard carbon anode, a smooth charge–discharge profile is obtained at an average operating voltage of approximately 2.75 V as seen in Fig. 37a. The full cell delivered a reversible capacity of 100 mA h g^{-1} (~0.46Na) for 150 cycles within the voltage range of 4.0–2.0 at 0.5 C and an excellent rate capability of 94 mA h g^{-1} at 1 C is achieved as seen in Fig. 37b.

5.2 $Na_x[NiCoMn]O_2$

A Na analogue of commercially available $LiNi_{1/3}Mn_{1/3}Co_{1/3}O_2$ (LiNMC), $NaNi_{1/3}Mn_{1/3}Co_{1/3}O_2$ (NaNMC), has been evaluated for Na-ion battery cathode materials.[100] Originating from the $Ni^{4+/2+}$ redox reaction, the cathode delivered a reversible capacity of 120 mA h g^{-1} (0.5Na) within the voltage range of 3.75–2.00 V at 0.1 C. However *in situ* XRD data analysis revealed that the electrode undergoes O3–O1–P3–P1 phase transition during the cycling, which appears as multiple plateaus in the charge–discharge profile in Fig. 38a. An excellent capacity retention as well as rate capability (Fig. 38b) is observed for 50 cycles within the voltage range of 3.75–2.5 V (Fig. 38b, inset) although when the cut-off voltage is raised to 4.2 V, the capacity reached more than 120 mA h g^{-1} at the expense of rapid capacity loss.

The stabilizing effect on the capacity retention of proton exchanged P2-phase $Na_{0.63}Ni_{0.22}Co_{0.11}Mn_{0.66}O_2$ is investigated by treating pristine material, in water, which causes sodium leaching and proton exchange.[101,23] As shown in Fig. 39a, the rinsed material shows lower discharge capacity during the first cycle but outperforms during the later cycles with higher capacity retention (95% for the rinsed material, 91% for the as-prepared material) at the 50th cycle along with 99.5% Coulombic efficiency after 15 cycles for rinsed material, which confirms the better stability of the rinsed material. Increased rate capability shown in Fig. 39a is also an indicative of the better stability of the proton exchanged material. Such an improvement proves that combining multiple transition metals induces a positive cooperative effect on the overall electrochemistry. The improvement of the overall electrochemical performance is suggested to be a result of more reversible P2–O2 phase transition for the proton exchanged material at high voltage. By stoichiometric calculation, 0.18 equivalent of Na^+ is exchanged by a proton. Supposing the total possible Na^+ concentration in interlayer space is 1.0, the ratio between the available interlayer position for Na^+ and the proton is 4.6 to 1. Therefore, the Na de/intercalation pathway should not be hindered to a large degree. Fig. 39b shows the extraordinary cycling performance of the proton exchanged material where the Coulombic efficiency raises up to 99.7% from the 50th to the 275th cycle and the capacity retention after 275 cycles reaches approximately 100 mA h g^{-1} which is 72% retention from the 2nd cycle.

Doping an electrochemically inactive element into a transition metal oxide layer is shown to improve the electrochemical performance in the case of P2-phase $Na_{0.67}[Mn_{0.65}Ni_{0.15}Co_{0.2}]O_2$ and $Na_{0.67}[Mn_{0.65}Ni_{0.15}Co_{0.15}Al_{0.05}]O_2$ microflakes.[102] The

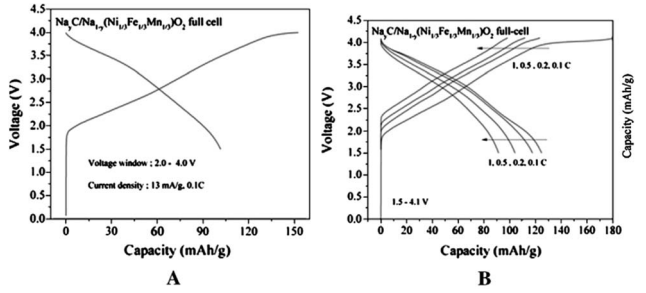

Fig. 37 (a) First cycle of a full Na-ion cell $Na_yC/Na_{1-y}[Ni_{1/3}Fe_{1/3}Mn_{1/3}]O_2$; (~0 < *y* < 0.7 (charge)), and (b) multiple cycle rate test of the cell (voltage windows and C rates are labeled in the figures; 1 C rate is 150 mA g^{-1}). Reprinted with permission from Elsevier: D. Kim, E. Lee, M. Slater, W. Lu, S. Rood and C. S. Johnson, *Electrochem. Commun.*, 2012, **18**, 66–69. Copyright 2012.

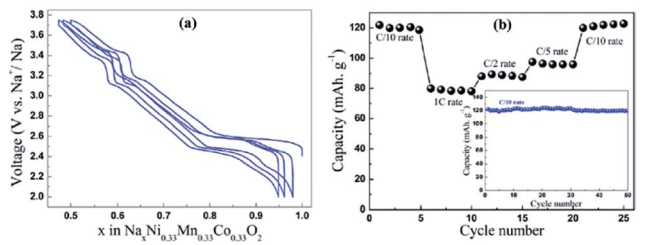

Fig. 38 (a) Voltage *vs.* composition profile of $NaNi_{1/3}Mn_{1/3}Co_{1/3}O_2$ as deduced from galvanostatic cycling at 0.1 C rate. (b) Rate capability plot showing cycling performance at various rates. The inset of (b) shows the plot of capacity retention with respect to cycle numbers. Reprinted with permission from American Chemical Society: M. Sathiya, K. Hemalatha, K. Ramesha, J.-M. Tarascon and A. S. Prakash, *Chem. Mater.*, 2012, **24**, 1846–1853. Copyright 2012.

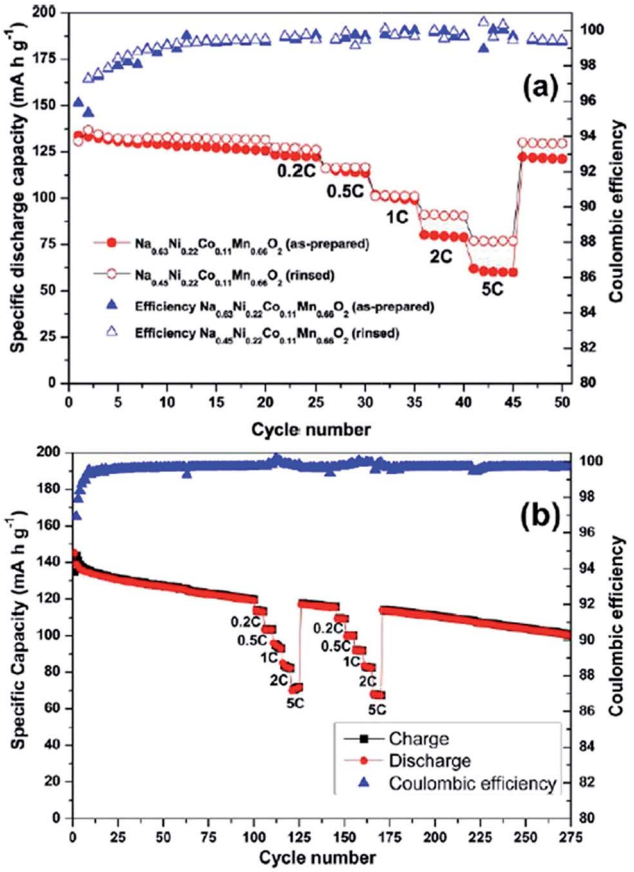

Fig. 39 (a) Specific discharge capacity and Coulombic efficiency during galvanostatic cycling of the as-prepared (filled markers) and rinsed (hollow markers) materials. Cut-off limits: 4.3–2.1 V (*vs.* Na/Na^+). Reference and counter electrodes: Na. Electrolyte: 0.5 M $NaPF_6$ in PC. Temperature: 20 ± 2 °C. Cycles 1 through 20 and 46 through 50 were performed at 0.1 C (12 mA g^{-1}). Cycles 21 through 45 illustrate the behavior during the *C*-rate test performed at 0.2 C (24 mA g^{-1}), 0.5 C (61 mA g^{-1}), 1 C (122 mA g^{-1}), 2 C (244 mA g^{-1}), and 5 C (610 mA g^{-1}). (b) Galvanostatic cycling at 0.1 C (12 mA g^{-1}) of the rinsed material, $Na_{0.45}Ni_{0.22}Co_{0.11}Mn_{0.66}O_2$. Cycles 101 through 125 and 146 through 170 illustrate the behavior during the *C*-rate test performed at 0.2 C (24 mA g^{-1}), 0.5 C (61 mA g^{-1}), 1 C (122 mA g^{-1}), 2 C (244 mA g^{-1}), and 5 C (610 mA g^{-1}). Reprinted with permission from American Chemical Society: D. Buchholz, A. Moretti, R. Kloepsch, S. Nowak, V. Siozios, M. Winter and S. Passerini, *Chem. Mater.*, 2013, **25**, 142–148. Copyright 2013.

charge–discharge profiles of both phases exhibit 3 voltage plateaus as shown in Fig. 40a and b, but the reversible capacity of the Al-doped cathode during the first few cycles is slightly lower than that of the undoped cathode. However the capacity retention improved vastly for the Al-doped cathode by retaining from 129 mA h g^{-1} to 123 mA h g^{-1} at the 50th cycle as seen in Fig. 40b. The cycling performances of the substituted and unsubstituted materials (Fig. 40c) show that the unsubstituted sample suffers from a significant discharge capacity loss during the first several cycles while the substituted sample does not exhibit a noticeable capacity fade. In addition, the rate capability shown in Fig. 40d proves that the substituted material can cycle at high *C*-rates by maintaining 50% of capacity at a current

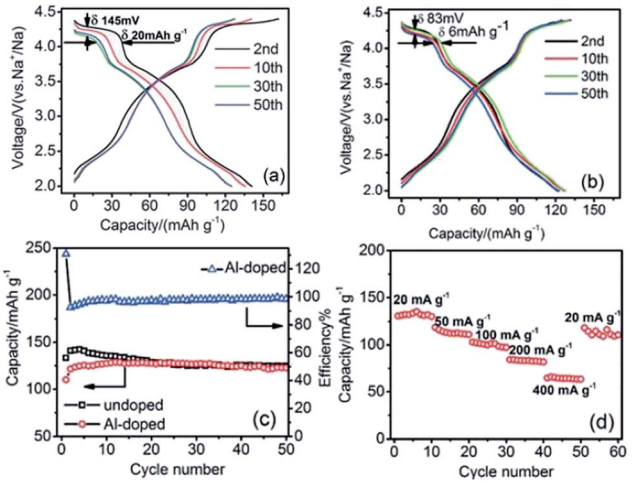

Fig. 40 Na-insertion/extraction properties of the NaMNC and NaMNCA microflakes: (a) charge–discharge curves cycled at 20 mA g^{-1} in the voltage interval of 4.4–2.0 V; (b) charge–discharge curves at selected cycles; (c) cycling performance of the NaMNC and NaMNCA electrodes at a constant current of 20 mA g^{-1}; (d) reversible capacities cycled at changing current rates as labeled. Reprinted with permission from The Royal Society of Chemistry: D. Yuan, W. He, F. Pei, F. Wu, Y. Wu, J. Qian, Y. Cao, X. Ai and H. Yang, *J. Mater. Chem. A*, 2013, **1**, 3895–3899. Copyright 2013.

density of 400 mA g^{-1}, which demonstrates unquestionable benefits by electrochemically inactive element substitution.

5.3 Li-rich layered oxide

In an effort to increase the specific capacity, the Li-rich layered oxide, $0.5Li_2MnO_3 \cdot 0.5LiMn_{0.42}Ni_{0.42}Co_{0.16}O_2$, as a Na-ion battery cathode has been evaluated by electrochemical Na-insertion.[21] Approximately 1.08Li is extracted and 0.76Na (239 mA h g^{-1}) is intercalated into the host structure within the voltage range of 4.5–1.7 V at a current density of 5 mA g^{-1}. The following charge capacity reached 244 mA h g^{-1} and the first three charge–discharge and CV curves overlap with each other very well, which indicates a good cyclability (Fig. 41a and b). Notice that the discharge capacity at an average voltage of 2.75 V results in an energy density of 644 W h kg^{-1}, which is higher than that of the commercially available Li-ion battery cathode. CV curves exhibit 3 highly reversible redox couples of O1/R1 at 4.2/3.5 V ($Co^{4+/3+}$), O2/R2 at 2.8/2.4 V ($Ni^{4+/2+}$), and O3/R3 at 2.3/1.8 V ($Mn^{4+/3+}$). The discharge capacities at the currents of 5, 10, 50, and 100 mA g^{-1} are 234, 224, 201, and 178 mA h g^{-1} (Fig. 41c), respectively and capacity retentions are 147 mA h g^{-1} after 45 cycles and 135 mA h g^{-1} after 54 cycles at a current of 50 and 100 mA h g^{-1}, respectively (Fig. 41d).

A similar approach has been explored using $Na_{0.95}Li_{0.15}(Ni_{0.15}Mn_{0.55}Co_{0.1})O_2$ by electrochemical insertion of Na utilizing a Li analogue.[22] Na intercalation induced 20% volume expansion and Mn, Ni, and Co redox peaks are clearly visible in the CV (Fig. 42a). The Na-system delivered the 1st discharge capacity of 220 mA h g^{-1} and the 2nd discharge capacity of 200 mA h g^{-1} when discharged to 2.0 V (Fig. 42c), and the 1st discharge capacity increased to 238 mA h g^{-1} when discharged

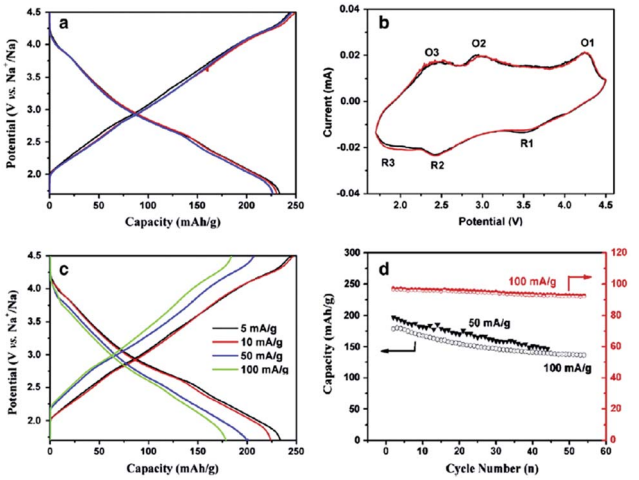

Fig. 41 (a) Curves of the first three charge–discharge profiles, (b) CV curves at a scan rate of 0.05 mV s^{-1} for the Na-rich layered oxide between 1.7 and 4.5 V s Na^+/Na, (c) charge–discharge profiles of the Na-rich layered oxide at different current densities, and (d) cycle performances at currents of 50 and 100 mA g^{-1}, and Coulombic efficiencies at a current of 100 mA g^{-1}. Reprinted with permission from Elsevier: Z. Jian, H. Yu and H. Zhou, *Electrochem. Commun.*, 2013, **34**, 215–218. Copyright 2013.

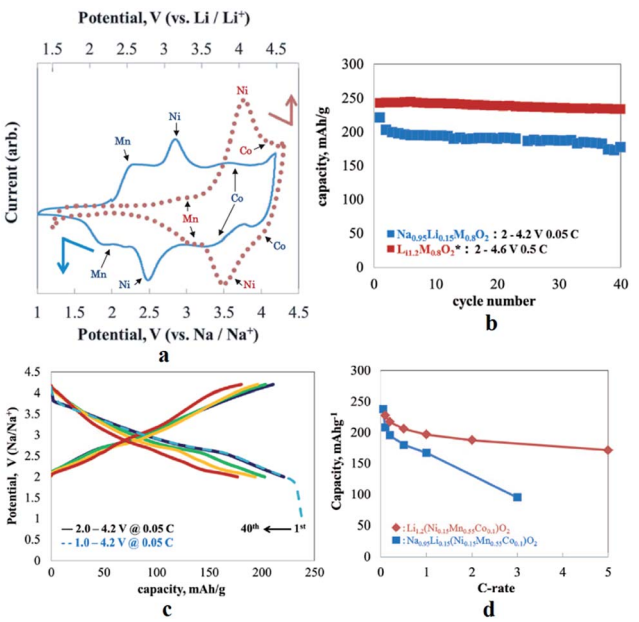

Fig. 42 (a) Cyclic voltammograms of samples $Li_{1.2}(Ni_{0.15}Mn_{0.55}Co_{0.1})O_2$ and $Na_{0.95}Li_{0.15}(Ni_{0.15}Mn_{0.55}Co_{0.1})O_2$ in the potential range from 1.5 to 4.6 V(Li/Li^+) for $Li_{1.2}(Ni_{0.15}Mn_{0.55}Co_{0.1})O_2$ and from 1 to 4.2 V (Na/Na^+) for $Na_{0.95}Li_{0.15}(Ni_{0.15}Mn_{0.55}Co_{0.1})O_2$. (b) Charge and discharge curves of $Na_{0.95}Li_{0.15}(Ni_{0.15}Mn_{0.55}Co_{0.1})O_2$ galvanostatically measured at the 0.05 C rate in the voltage ranges of 2.0–4.2 V (solid line) and 1.0–4.2 V (dashed line). (C) Cycling performances of samples $Li_{1.2}(Ni_{0.15}Mn_{0.55}Co_{0.1})O_2$ and $Na_{0.95}Li_{0.15}(Ni_{0.15}Mn_{0.55}Co_{0.1})O_2$. (d) Charge and discharge curves of sample $Li_{1.2}(Ni_{0.15}Mn_{0.55}Co_{0.1})O_2$ at various current densities (0.05–3 C). Reprinted with permission from The Electrochemical Society: R. Kataoka, T. Mukai, A. Yoshizawa and T. Sakai, *J. Electrochem. Soc.*, 2013, **160**, A933–A939. Copyright 2013.

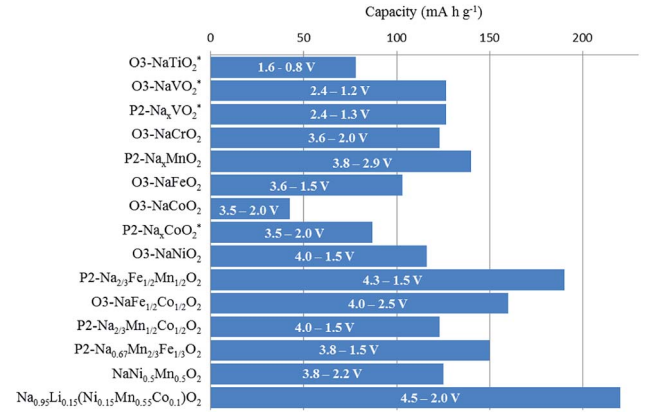

Fig. 43 Reversible capacity of selected layered oxides reported in the literature. * indicates capacity estimated by the number of reversible Na. The reversible capacities of all P2-phases are based on the 1st discharge or beyond. The voltage window of each material is indicated in the bar.

to 1.0 V (Fig. 42c). Also, the Na-based system exhibited a moderate capacity retention of 170 mA h g^{-1} up to 40 cycles (Fig. 42b) along with the rate capability of 167 mA h g^{-1} at 1 C.

6. Conclusion

Fig. 43 includes the electrochemical performance of some of the significant Na layered oxides published to date. It should be noted that some of the capacities are well within the range of today's commercially available secondary battery.

Despite the extensive research showing much improvement of overall electrochemistry, many aspects need to be addressed. In this review, 4 major challenges are recognized.

(1) Low operating voltage: the challenge lies in the fact that the redox reaction of each T_M has its unique potential. One approach to address this issue is to include the elements with higher redox potential such as $Fe^{3+/4+}$. However, it is shown that utilizing an extensive amount of $Fe^{3+/4+}$ redox reaction may result in structural instability.

(2) Na deficiency of the P2-phase: although the P2-phase produces much more stable electrochemical cycling due to structural stability, the major challenge is that the P2-phase can only be stabilized at low Na concentrations in the pristine state. As seen in some recent literature this issue can be partially addressed by utilizing sacrificial salts such as NaN_3. The search for new sacrificial salts (*e.g.* NaC_2O_4) that could have similar electrochemical properties to those of NaN_3 can further address such issues.

(3) Long term stability of host structure: the possibilities of undergoing multiple phase transitions during the charge–discharge cycle imply the structural instability during a long term cycling. Recent literature, however, showed possibilities to improve the structural stability by substituting with electrochemically inactive elements such as Mg, and this strategy should be further investigated with other suitable elements.

(4) High polarization: the high polarization issue of Na layered oxide materials has not been focused much up to date,

but could be a major obstacle in the near future. First, insight into the cause of this issue must be investigated in more detail before deploying any strategic approach to address this issue. Reducing the size of the electrode particle and optimization of the electrode slurry composition would be some quick approaches to decrease the polarization.

The substitution strategies will be emphasized as they have provided a significant improvement in overall electrochemical performance, and improving the operating voltage and long term stability should be the main focuses. However, a balance between the average voltage, specific capacity, and long term capacity retention must be carefully considered when determining specific systems based on specific requirements for individual applications.

Acknowledgements

This work was financially supported by Ministerio de Economía y Competitividad (Proyecto I+D. Retos 2013), reference number: ENE 2013-44330-R and FPDI-2013-17329, and the Gobierno Vasco/EuskoJaurlaritza (Etortek CICEnergigune 10, SAIOTEK-12 ENERGIBA and IT570-13).

References

1 M. Armand and J.-M. Tarascon, *Nature*, 2008, **451**, 652–657.
2 V. Palomares, P. Serras, I. Villaluenga, K. B. Hueso, J. Carretero-González and T. Rojo, *Energy Environ. Sci.*, 2012, **5**, 5884–5901.
3 K. B. Hueso, M. Armand and T. Rojo, *Energy Environ. Sci.*, 2013, **6**, 734–749.
4 H. Pan, Y.-S. Hu and L. Chen, *Energy Environ. Sci.*, 2013, **6**, 2338–2360.
5 K. Kubota, N. Yabuuchi, H. Yoshida, M. Dahbi and S. Komaba, *MRS Bull.*, 2014, **39**, 416–422.
6 J. Xu, D. H. Lee and Y. S. Meng, *Funct. Mater. Lett.*, 2013, **6**, 1330001.
7 S.-W. Kim, D.-H. Seo, X. Ma, G. Ceder and K. Kang, *Adv. Energy Mater.*, 2012, **2**, 710–721.
8 B. L. Ellis and L. F. Nazar, *Curr. Opin. Solid State Mater. Sci.*, 2012, **16**, 168–177.
9 M. D. Slater, D. Kim, E. Lee and C. S. Johnson, *Adv. Funct. Mater.*, 2013, **23**, 947–958.
10 S. Engelke, *Storage4*, 2013, **1**, 1–7.
11 V. Palomares, M. Casas-Cabanas, E. Castillo-Martínez, M. H. Han and T. Rojo, *Energy Environ. Sci.*, 2013, **6**, 2312–2337.
12 C. Delmas, J.-J. Braconnier, C. Fouassier and P. Hagenmuller, *Solid State Ionics*, 1981, **3/4**, 165–169.
13 J. J. Braconnier, C. Delmas and P. Hagenmuller, *Mater. Res. Bull.*, 1982, **17**, 993–1000.
14 S. Miyazaki, S. Kikkawa and M. Koizumi, *Synth. Met.*, 1983, **6**, 211–271.
15 A. Maazaz, C. Delmas and P. Hagenmuller, *J. Inclusion Phenom.*, 1983, **1**, 45–51.
16 S. Kikkawa, S. Miyazaki and M. Koizumi, *Mater. Res. Bull.*, 1985, **20**, 373–377.
17 A. Mendiboure, C. Delmas and P. Hagenmuller, *J. Solid State Chem.*, 1985, **57**, 323–331.
18 J. Molenda, A. Stokłosa and D. Than, *Solid State Ionics*, 1987, **24**, 33–38.
19 L. W. Shacklette, T. R. Jow and L. Townsend, *J. Electrochem. Soc.*, 1988, **135**, 2669–2674.
20 N. Yabuuchi, A. Kajiyama, J. Iwatate, H. Nishikawa, S. Hitomi, R. Okuama, R. Usui, Y. Yamada and S. Komaba, *Nat. Mater.*, 2012, **11**, 512–517.
21 Z. Jian, H. Yu and H. Zhou, *Electrochem. Commun.*, 2013, **34**, 215–218.
22 R. Kataoka, T. Mukai, A. Yoshizawa and T. Sakai, *J. Electrochem. Soc.*, 2013, **160**, A933–A939.
23 D. Buchholz, A. Moretti, R. Kloepsch, S. Nowak, V. Siozios, M. Winter and S. Passerini, *Chem. Mater.*, 2013, **25**, 142–148.
24 S. Komaba, W. Murata, T. Ishikawa, N. Yabuuchi, T. Ozeki, T. Nakayama, A. Ogata, K. Gotoh and K. Fujiwara, *Adv. Funct. Mater.*, 2011, **21**, 3859–3867.
25 X. Wang, G. Liu, T. Iwao, M. Okubo and A. Yamada, *J. Phys. Chem. C*, 2014, **118**, 2970–2976.
26 S. Komaba, N. Yabuuchi, T. Nakayama, A. Ogata, T. Ishikawa and I. Nakai, *Inorg. Chem.*, 2012, **51**, 6211–6220.
27 C. Delmas, C. Fouassier and P. Hagenmuller, *Physica B+C*, 1980, **99**, 81–85.
28 P. Vassilaras, X. Ma, X. Li and G. Ceder, *J. Electrochem. Soc.*, 2013, **160**, A207–A211.
29 A. Mendiboure, C. Delmas and P. Hagenmuller, *J. Solid State Chem.*, 1985, **57**, 323–331.
30 I. Saadoune, A. Maazaz, M. Ménétrier and C. Delmas, *J. Solid State Chem.*, 1996, **122**, 111–117.
31 D. H. Lee, J. Xu and Y. S. Meng, *Phys. Chem. Chem. Phys.*, 2013, **15**, 3304–3312.
32 D. Hamani, M. Ati, J.-M. Tarascon and P. Rozier, *Electrochem. Commun.*, 2011, **13**, 938–941.
33 M. Guignard, C. Didier, J. Darriet, P. Bordet, E. Elkaïm and C. Delmas, *Nat. Mater.*, 2013, **12**, 74–80.
34 C. Didier, M. Guignard, J. Darriet and C. Delmas, *Inorg. Chem.*, 2012, **51**, 11007–11016.
35 C. Didier, M. Guignard, C. Denage, O. Szajwaj, S. Ito, I. Saadoune, J. Darriet and C. Delmas, *Electrochem. Solid-State Lett.*, 2011, **14**, A75–A78.
36 S. Komaba, C. Takei, T. Nakayama, A. Ogata and N. Yabuuchi, *Electrochem. Commun.*, 2010, **12**, 355–358.
37 X. Xia and J. R. Dahn, *Electrochem. Solid-State Lett.*, 2011, **15**, A1–A4.
38 J.-J. Ding, Y.-N. Zhou, Q. Sun and Z.-W. Fu, *Electrochem. Commun.*, 2012, **22**, 85–88.
39 C.-Y. Chen, K. Matsumoto, T. Nohira, R. Hagiwara, A. Fukunaga, S. Sakai, K. Jitta and S. Inazawa, *J. Power Sources*, 2013, **237**, 52–57.
40 M. M. Doeff, T. J. Richardson, J. Hollingsworth, C.-W. Yuan and M. Gonzales, *J. Power Sources*, 2002, **112**, 294–297.
41 F. Sauvage, L. Laffont, J.-M. Tarascon and E. Baudrin, *Inorg. Chem.*, 2007, **46**, 3289–3294.
42 J. A. Saint, M. M. Doeff and J. Wilcox, *Chem. Mater.*, 2008, **20**, 3404–3411.

43 J. F. Whitcare, A. Tevar and S. Sharma, *Electrochem. Commun.*, 2010, **12**, 463–466.
44 A. D. Tevar and J. F. Whitcare, *J. Electrochem. Soc.*, 2010, **157**, A870–A875.
45 J.-P. Parant, R. Olazcuaga, M. Devalette, C. Fouassier and P. Hagenmuller, *J. Solid State Chem.*, 1971, **3**, 1–11.
46 X. Li, X. Ma, D. Su, L. Liu, R. Chisnell, S. P. Ong, H. Chen, A. Toumar, J.-C. Idrobo, Y. Lei, J. Bai, F. Wang, J. W. Lynn, Y. S. Lee and G. Ceder, *Nat. Mater.*, 2014, **13**, 586–592.
47 X. Ma, H. Chen and G. Ceder, *J. Electrochem. Soc.*, 2011, **158**, A1307–A1312.
48 A. Caballero, L. Hernán, J. Morales, L. Sánchez, J. Santos Peña and M. A. G. Aranda, *J. Mater. Chem.*, 2002, **12**, 1142–1147.
49 J. M. Paulsen and J. R. Dahn, *Solid State Ionics*, 1999, **126**, 3–24.
50 D. Su, C. Wang, H. Ahn and G. Wang, *Chem.–Eur. J.*, 2013, **19**, 10884–10889.
51 J. Billaud, G. Singh, A. R. Armstrong, E. Gonzalo, V. Roddatis, C. Armand, T. Rojo and P. G. Bruce, *Energy Environ. Sci.*, 2014, **7**, 1387–1391.
52 N. Yabuuchi, R. Hara, K. Kubota, J. Paulsen, S. Kumakura and S. Komaba, *J. Mater. Chem. A*, 2014, **40**, 16851–16855.
53 Y. Takeda, J. Akagi, A. Edagawa, M. Inagaki and S. Naka, *Mater. Res. Bull.*, 1980, **15**, 1167–1172.
54 S. Kikkawa, S. Miyazaki and M. Koizumi, *Mater. Res. Bull.*, 1985, **20**, 373–377.
55 Y. Takeda, K. Nakahara, M. Nishijima, N. Imanishi and O. Yamamoto, *Mater. Res. Bull.*, 1994, **29**, 659–666.
56 M. C. Blesa, E. Morana, C. León, J. Santamaria, J. D. Tornero and N. Menéndez, *Solid State Ionics*, 1999, **126**, 81–87.
57 C. Delmas, A. Maazaz, C. Fouassier, J. M. Reau and P. Hagenmuller, *Mater. Res. Bull.*, 1979, **14**, 329–335.
58 N. Yabuuchi, H. Yoshida and S. Komaba, *Electrochemistry*, 2012, **80**, 716–719.
59 J. Zhao, L. Zhao, N. Dimov, S. Okada and T. Nishida, *J. Electrochem. Soc.*, 2013, **160**, A3077–A3081.
60 T. Shirane, R. Kanno, Y. Kawamoto, Y. Takeda, M. Takano, T. Kamiyama and F. Izumi, *Solid State Ionics*, 1995, **79**, 227–233.
61 J. Morales, J. Santos-Peña, R. Trócoli, S. Franger and E. Rodríguez-Castelló, *Electrochim. Acta*, 2008, **53**, 6366–6371.
62 Y. S. Lee, S. Sato, Y. K. Sun, K. Kobayakawa and Y. Sato, *J. Power Sources*, 2003, **119**, 285–289.
63 J. Zhang, J.-Z. Wang, S.-L. Chou, U.-K. Liu, K. Ozawa and J.-J. Li, *Electrochim. Acta*, 2013, **108**, 820–826.
64 C. Delmas, J. Braconnier, C. Fouassier and P. Hagenmuller, *Solid State Ionics*, 1981, **3–4**, 165–169.
65 R. Berthelot, D. Carlier and C. Delmas, *Nat. Mater.*, 2011, **10**, 74–80.
66 J. J. Ding, Y. N. Zhou, Q. Sun, X. Q. Yu, X. Q. Yang and Z. W. Fu, *Electrochim. Acta*, 2013, **87**, 388–393.
67 A. K. Rai, L. T. Anh, J. Gim, V. Mathew and J. Kim, *Ceram. Int.*, 2014, **40**, 2411–2417.
68 M. D'Arienzo, R. Ruffo, R. Scotti, F. Morazzoni, C. M. Mari and S. Polizzi, *Phys. Chem. Chem. Phys.*, 2012, **14**, 5945–5952.
69 A. Bhide and K. Hariharan, *Solid State Ionics*, 2011, **192**, 360–363.
70 Y. Ma, M. M. Doeff, S. J. Visco and L. C. De Jonghe, *J. Electrochem. Soc.*, 1993, **140**, 2726–2733.
71 R. Alcántara, J. M. Jiménez-Mateos, P. Lavela and J. L. Tirado, *Electrochem. Commun.*, 2001, **3**, 639–642.
72 J. Molenda and A. Stoklosa, *Solid State Ionics*, 1990, **38**, 1–4.
73 M. H. Han, E. Gonzalo, M. Casas-Cabanas and T. Rojo, *J. Power Sources*, 2014, **258**, 266–271.
74 J. Baker, R. J. Heap, N. Roche, C. Tan, R. Sayers and Y. Liu, *High Performance Na-ion Batteries Based on Novel O3 Layered Oxide Cathode Materials*, International Meeting on Lithium Batteries, Como, Italy, 2014.
75 J. Gopalakrishnan, *Bull. Mater. Sci.*, 1985, **7**, 201–214.
76 H. Wang, B. Yang, X.-Z. Liao, J. Xu, D. Yang, D. Yang, Y.-S. He and Z.-F. Ma, *Electrochim. Acta*, 2013, **113**, 200–204.
77 Z. Lu and J. R. Dahn, *J. Electrochem. Soc.*, 2001, **148**, A1225–A1229.
78 N. Yabuuchi, M. Yano, H. Yoshida, S. Kuze and S. Komaba, *J. Electrochem. Soc.*, 2013, **160**, A3131–A3137.
79 H. Yoshida, N. Yabuuchi, K. Kubota, I. Ikeuchi, A. Garsuch, M. Schulz-Dobrick and S. Komaba, *Chem. Commun.*, 2014, **50**, 3677–3680.
80 H. Yu, S. Guo, Y. Zhu, M. Ishida and H. Zhou, *Chem. Commun.*, 2014, **50**, 457–459.
81 S. Okada, J. Yamaki, Y. Takahashi and K. Nakane, *EU Pat.*, EP 1 826 845 A1, 2007.
82 D. Kim, S.-H. Kang, M. Slater, S. Rood, J. T. Vaughey, N. Karan, M. Balasubramanian and C. S. Johnson, *Adv. Energy Mater.*, 2011, **1**, 333–336.
83 J. Cho, T.-J. Kim, Y. J. Kim and B. Park, *Chem. Commun.*, 2001, 1074–1075.
84 N. Yabuuchi and S. Komaba, *Sci. Technol. Adv. Mater.*, 2014, **15**, 043501–043530.
85 J. Xu, S.-L. Chou, J.-L. Wang, H.-K. Liu and S.-S. Dou, *ChemElectroChem*, 2014, **1**, 371–374.
86 J. S. Thorne, R. A. Dunlap and M. N. Obrovac, *J. Electrochem. Soc.*, 2013, **160**, A361–A367.
87 Z. Yuan, W. Xuehang, W. Wenwei and W. Kaitu, *Ceram. Int.*, 2014, **40**, 13679–13682.
88 J. Zhao, J. Xu, D. H. Lee, N. Dimov, Y. S. Meng and S. Okada, *J. Power Sources*, 2014, **264**, 235–239.
89 G. Singh, B. Acebedo, M. Casas Cabanas, D. Shanmukaraj, M. Armand and T. Rojo, *Electrochem. Commun.*, 2013, **37**, 61–63.
90 G. Singh, F. Aguesse, L. Otaegui, E. Goikolea, E. Gonzalo, J. Segalini and T. Rojo, *J. Power Sources*, 2015, **273**, 333–339.
91 M. Yoncheva, R. Stoyanova, E. Zhecheva, E. Kuzmanova, M. Sendova-Vassileva, D. Nihtianova, D. Carlier, M. Guignard and C. Delmas, *J. Mater. Chem.*, 2012, **22**, 23418–23427.
92 H. Yoshida, N. Yabuuchi and S. Komaba, *Electrochem. Commun.*, 2013, **34**, 60–63.

93 D. Carlier, J. H. Cheng, R. Berthelot, M. Guignard, M. Yoncheva, R. Stoyanova, B. J. Hwang and C. Delmas, *Dalton Trans.*, 2011, 9306–9312.
94 X. Wang, M. Tamaru, M. Okubo and A. Yamada, *J. Phys. Chem. C*, 2013, **117**, 15545–15551.
95 N. Bucher, S. Hartung, I. Gocheya, Y. L. Cheah, M. Srinivasan and H. E. Hoster, *J. Solid State Electrochem.*, 2013, **17**, 1923–1929.
96 D. Yuan, X. Hu, J. Qian, F. Pei, F. Wu, R. Mao, X. Ai, H. Yang and Y. Cao, *Electrochim. Acta*, 2014, **116**, 300–305.
97 I. Hasa, D. Buchholz, S. Passerini, B. Scrosati and J. Hassoun, *Adv. Energy Mater.*, 2014, **4**, 1400083–1400089.
98 X. Sun, Y. Jin, C.-Y. Zhang, J.-W. Wen, Y. Shao, Y. Zhang and C.-H. Chen, *J. Mater. Chem. A*, 2014, **2**, 17268–17271.
99 D. Kim, E. Lee, M. Slater, W. Lu, S. Rood and C. S. Johnson, *Electrochem. Commun.*, 2012, **18**, 66–69.
100 M. Sathiya, K. Hemalatha, K. Ramesha, J.-M. Tarascon and A. S. Prakash, *Chem. Mater.*, 2012, **24**, 1846–1853.
101 D. Buchholz, L. G. Chagas, M. Winter and S. Passerini, *Electrochim. Acta*, 2013, **110**, 208–213.
102 D. Yuan, W. He, F. Pei, F. Wu, Y. Wu, J. Qian, Y. Cao, X. Ai and H. Yang, *J. Mater. Chem. A*, 2013, **1**, 3895–3899.